Received: 25 March 2023 | Revised: 27 June 2023 | Accepted: 10 August 2023

DOI: 10.1002/hbm.26471

RESEARCH ARTICLE

WILEY

Denoising brain networks using a fixed mathematical phase change in independent component analysis of magnitude-only fMRI data

Chao-Ying Zhang[1] | Qiu-Hua Lin[1] | Yan-Wei Niu[1] | Wei-Xing Li[1] | Xiao-Feng Gong[1] | Fengyu Cong[2,3] | Yu-Ping Wang[4] | Vince D. Calhoun[5]

[1]School of Information and Communication Engineering, Faculty of Electronic Information and Electrical Engineering, Dalian University of Technology, Dalian, China

[2]School of Biomedical Engineering, Faculty of Electronic Information and Electrical Engineering, Dalian University of Technology, Dalian, China

[3]Faculty of Information Technology, University of Jyväskylä, Jyväskylä, Finland

[4]Tulane University, Biomedical Engineering Department, New Orleans, Louisiana, USA

[5]Tri-institutional Center for Translational Research in Neuroimaging and Data Science (TReNDS), Georgia State University, Georgia Institute of Technology, Emory University, Atlanta, Georgia, USA

Correspondence
Qiu-Hua Lin, School of Information and Communication Engineering, Faculty of Electronic Information and Electrical Engineering, Dalian University of Technology, Dalian 116024, China.
Email: qhlin@dlut.edu.cn

Funding information
National Natural Science Foundation of China, Grant/Award Numbers: 61871067, 61379012, 61671106, 62071082, 81471742; National Science Foundation, Grant/Award Number: 2112455; National Institutes of Health, Grant/Award Numbers: R01EB005846, R01MH107354, R01MH104680; Fundamental Research Funds for the Central Universities, China, Grant/Award Number: DUT20ZD220; Supercomputing Center of Dalian University of Technology

Abstract

Brain networks extracted by independent component analysis (ICA) from magnitude-only fMRI data are usually denoised using various amplitude-based thresholds. By contrast, spatial source phase (SSP) or the phase information of ICA brain networks extracted from complex-valued fMRI data, has provided a simple yet effective way to perform the denoising using a fixed phase change. In this work, we extend the approach to magnitude-only fMRI data to avoid testing various amplitude thresholds for denoising magnitude maps extracted by ICA, as most studies do not save the complex-valued data. The main idea is to generate a mathematical SSP map for a magnitude map using a mapping framework, and the mapping framework is built using complex-valued fMRI data with a known SSP map. Here we leverage the fact that the phase map derived from phase fMRI data has similar phase information to the SSP map. After verifying the use of the magnitude data of complex-valued fMRI, this framework is generalized to work with magnitude-only data, allowing use of our approach even without the availability of the corresponding phase fMRI datasets. We test the proposed method using both simulated and experimental fMRI data including complex-valued data from University of New Mexico and magnitude-only data from Human Connectome Project. The results provide evidence that the mathematical SSP denoising with a fixed phase change is effective for denoising spatial maps from magnitude-only fMRI data in terms of retaining more BOLD-related activity and fewer unwanted voxels, compared with amplitude-based thresholding. The proposed method provides a unified and efficient SSP approach to denoise ICA brain networks in fMRI data.

KEYWORDS
fMRI, independent component analysis, denoising, mathematical spatial source phase, mapping framework, fixed phase change

1 | INTRODUCTION

Independent component analysis (ICA) has been widely used to extract brain networks from functional magnetic resonance imaging (fMRI) data, and these brain networks or ICA spatial maps are often denoised by amplitude-based thresholding in the analyses of magnitude-only fMRI data. For multiple subjects or single-subject with multiple runs, the amplitude thresholds can be readily computed using a one sample *t*-test to identify significant source voxels in the ICA spatial maps at a predefined significant level, for example, $p < .05$–$.001$ (Abou et al., 2010; Afshin-Pour et al., 2014; Calhoun, Adalı, Pearlson, et al., 2001a; Calhoun & Pearlson, 2012; Erhardt et al., 2011; Goebel et al., 2006; Gopinath et al., 2019; Kuang, Lin, Gong, Cong, et al., 2017b; Wu & Calhoun, 2023). However, such statistical evaluation is unsuitable for determining the threshold when denoising a single ICA brain network. The single ICA brain network is usually obtained by three ways. The first way is by the ICA of single-subject fMRI data at a single run or at the best run, which is selected from multiple runs based on a specific criterion (Brookes et al., 2011; Calhoun, Adalı, Pearlson, et al., 2001b; Calhoun & de Lacy, 2017; Correa et al., 2005; Damoiseaux et al., 2007; Jung et al., 2001; Kuang, Lin, Gong, Cong, et al., 2017a; Li et al., 2007; Long et al., 2009; McKeown et al., 1998; Risk et al., 2013; Sui et al., 2012; Yu et al., 2015). The second way is by averaging ICA spatial maps across multiple subjects (Calhoun, Adalı, Mcginty, et al., 2001; Kuang et al., 2018; Kuang, Lin, Gong, Chen, et al., 2017; Kuang, Lin, Gong, Cong, et al., 2017b; Shi & Zeng, 2018). The third one is by detecting a shared brain network via the temporally concatenated group ICA (Britz et al., 2010; Calhoun et al., 2009; Calhoun & de Lacy, 2017; Erhardt et al., 2011; Qi et al., 2019; Qin et al., 2018; Shi et al., 2018), or via the tensor decomposition of multiple-subject fMRI data (Acar et al., 2019; Beckmann & Smith, 2005; Han et al., 2022; Kuang et al., 2015, 2020; Mørup et al., 2008; Wolf et al., 2010; Zhou et al., 2016). In these situations, amplitude-based thresholding in terms of *z*-score is widely used for denoising ICA brain networks. Indeed, this *z*-score threshold was used in the first publication by McKeown et al. (1998). The source voxels above a predefined *z*-score threshold are recognized as the desired voxels in a brain network. With the significantly increasing studies in ICA of magnitude-only fMRI data, the *z*-score thresholds varied with different analyses, possibly due to different considerations such as for clearer visualization and closer to the reference. For example, *z*-score thresholds from 1 to 3 were predefined for denoising ICA spatial maps from a single subject (Brookes et al., 2011; Calhoun, Adalı, Pearlson, et al., 2001b; Calhoun & de Lacy, 2017; Correa et al., 2005; Damoiseaux et al., 2007; Jung et al., 2001; Kuang, Lin, Gong, Cong, et al., 2017a; Li et al., 2007; Long et al., 2009; Schwartz et al., 2019; Sui et al., 2012; Yu et al., 2015); *z*-score thresholds ranging from 0.5 to 2.5 were used for denoising an averaged ICA spatial map across multiple subjects (Calhoun, Adalı, Mcginty, et al., 2001; Kuang et al., 2018; Kuang, Lin, Gong, Chen, et al., 2017; Kuang, Lin, Gong, Cong, et al., 2017b; Shi & Zeng, 2018; Yu et al., 2015); and *z*-score thresholds from 0.5 to 2.7 were used for denoising a shared spatial map obtained by the temporally concatenated group ICA (Britz et al., 2010; Calhoun et al., 2009; Calhoun & de Lacy, 2017; Erhardt et al., 2011; Qi et al., 2019; Qin et al., 2018; Shi et al., 2018) or by the tensor decomposition of multiple-subject fMRI data (Acar et al., 2019; Han et al., 2022; Kuang et al., 2015, 2020; Wolf et al., 2010).

In comparison with various amplitude (*z*-score) thresholds utilized for denoising ICA spatial maps from magnitude-only fMRI data, a fixed phase change $\Delta\varphi$, provides a simple yet effective measure to denoise highly noisy complex-valued maps extracted via ICA of complex-valued fMRI data (Lin et al., 2022; Yu et al., 2015). Spatial source phase (SSP), the phase of a source voxel in the ICA complex-valued map (Qiu et al., 2019), is such a measure that identifies blood oxygenation-level dependent (BOLD) related voxels in terms of their phase changes unrelated to their amplitudes. Different from the meaningless phase changes for the random complex Gaussian noise, as shown in Figure 1, smaller SSP phase changes ($\Delta\varphi \leq \pi/4$) correspond to BOLD-related voxels, whereas larger SSP phase changes

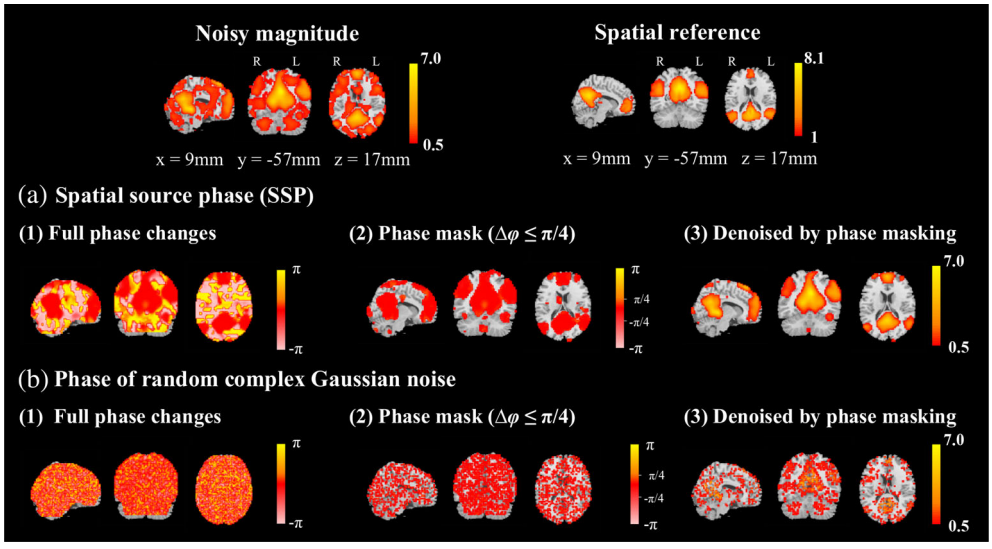

FIGURE 1 Different meaning of phase changes for (a) SSP and (b) the phase of random complex Gaussian noise in denoising an ICA complex-valued map (DMN). (1) Full phase changes $[-\pi, \pi]$, (2) phase mask with phase changes $\Delta\varphi \leq \pi/4$, and (3) magnitude map denoised by phase masking. The noisy magnitude map and spatial reference of DMN are shown at the top.

($\Delta\varphi > \pi/4$) are unwanted voxels (Lin et al., 2022; Yu et al., 2015), after removing the phase ambiguity of an ICA complex-valued map. Based on this, a fixed phase change ($\Delta\varphi = \pi/4$) has been used to generate a binary mask in the SSP denoising of ICA spatial maps for both task-related and resting-state fMRI data (Iqbal et al., 2020; Kuang et al., 2020; Kuang, Lin, Gong, Cong, et al., 2017a; Lin et al., 2022; Qiu et al., 2019; Song et al., 2021). More desired voxels can remain when using a large phase change $\Delta\varphi = \pi/4$ than using a smaller one ($\Delta\varphi < \pi/4$). A large number of unwanted voxels (in practice 60%–70% of the full phase changes) are removed, including those with larger amplitudes that cannot be removed using amplitude-based thresholding.

Meanwhile, many weak BOLD-related voxels (e.g., *z*-score threshold = 0.5) are detected to provide additional brain activity beyond magnitude-only fMRI data (Kuang et al., 2016, 2020; Kuang, Lin, Gong, Cong, et al., 2017a, b; Yu et al., 2015). Taking analyses of motor task-related complex-valued fMRI data as examples, 139% more contiguous motor-related voxels were detected for the task-related brain network as well as 331% more contiguous voxels were detected in the regions expected to be activated for the default mode network (DMN) in ICA of single-subject data (Yu et al., 2015); 393% more contiguous and reasonable activations were extracted for the task-related brain network and 301% for DMN in independent vector analysis of multiple-subject data (Kuang, Lin, Gong, Cong, et al., 2017b); and 178.7% more contiguous activations were detected in task-related regions consisting of the left and right primary motor areas and the supplementary motor areas in tensor decomposition of multiple-subject data (Kuang et al., 2020). These are consistent with the improved sensitivity and activation detection results obtained by model-driven (Rowe, 2005, 2009; Rowe & Logan, 2004; Yu et al., 2018, 2022) and data-driven (Arja et al., 2010; Calhoun & Adalı, 2012a; Calhoun et al., 2002) methods for analyzing complex-valued fMRI data, supporting the fact that fMRI phase contains biological information regarding the vasculature contained within voxels (Adrian et al., 2018; Feng et al., 2009; Yu et al., 2018, 2022). The effectiveness of SSP denoising is also consistent with previous findings that the phase change of observed phase fMRI data has the capacity of accessing the voxel quality. The desired microvascular response exhibits relatively smaller phase changes over time (Menon, 2002; Nencka & Rowe, 2007; Tomasi & Caparelli, 2007), and good-quality activation areas exhibit low phase variations when comparing to their surroundings such as skull and background of the fMRI slices (Feng et al., 2009; Rodriguez et al., 2011).

Motivated by the success of a fixed SSP threshold in denoising complex-valued spatial maps, we extend it to magnitude-only fMRI data, as most studies do not save the complex-valued fMRI data. To this end, we propose to get similar SSP values, namely mathematical SSP, for each ICA magnitude map derived from magnitude-only fMRI data. The development of mathematical SSP is reasonable because we have complex-valued fMRI data with known SSP maps as the reference. Figure 2 shows an overview of the proposed method. Here we leverage the fact that similar source phase information can be obtained from either the complex-valued fMRI data via complex ICA (i.e., SSP map) or the phase data via real ICA (i.e., phase map), and ICA phase/magnitude maps exhibit super-Gaussian distribution since the underlying fMRI sources are typically sparse (Calhoun & Adalı, 2012a, b; Ge et al., 2015, see also Figures S1–S3). By using complex-valued fMRI data and assuming similar super-Gaussian

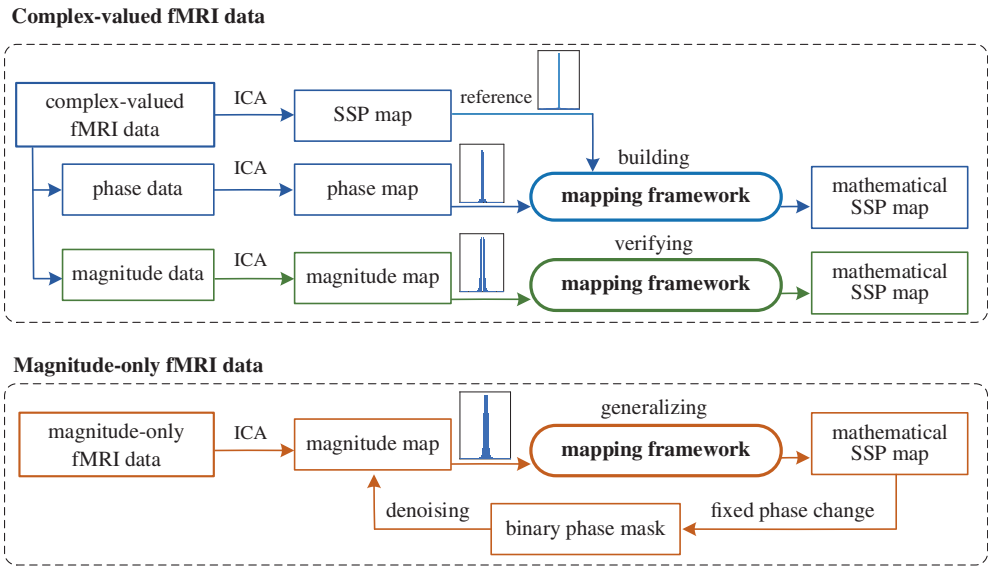

FIGURE 2 An overview of the proposed method. The mapping framework is used to generate a mathematical spatial source phase (SSP) map for a magnitude map from magnitude-only fMRI data (see the lower panel), the mathematical SSP map is sequentially used to denoise the magnitude map with a binary mask for a fixed phase change. The mapping framework is built using complex-valued fMRI data with a known SSP map (see the upper panel), leveraging the fact that the SSP map and the phase map (from phase data) have similar phase information or similar super-Gaussian distribution. The mapping framework is generalized to work with magnitude-only fMRI data after verifying the use of the magnitude data of complex-valued fMRI.

distribution between the SSP maps and the phase maps, we propose a reliable mapping framework comprising three stages: building, verifying and generalizing. First, we build the mapping framework for transforming a phase map into a mathematical SSP map. Second, we verify it using the magnitude data of complex-valued fMRI. Third, we generalize this mapping framework to deal with magnitude-only data, allowing use of our approach even without the availability of the corresponding phase fMRI datasets. Finally, we demonstrate the effectivity of mathematical SSP denoising using both simulated and experimental fMRI data including complex-valued data from the University of New Mexico (UNM) and the magnitude-only data from the Human Connectome Project (HCP, n.d.), in comparison to amplitude-based thresholding at three different *z*-score thresholds.

2 | MATERIALS AND METHODS

2.1 | Materials

2.1.1 | Simulated fMRI data

We generated simulated resting-state complex-valued fMRI data based on the linear mixing model used in SimTB (Erhardt et al., 2012) as follows:

$$\mathbf{Z}^k = \mathbf{A}^k \mathbf{S}^k + \mathbf{B}^k, \quad (1)$$

where $\mathbf{S}^k = \{\mathbf{s}_c^k\} \in \mathbb{C}^{C \times V}$ and $\mathbf{A}^k = \{\mathbf{a}_c^k\} \in \mathbb{C}^{T \times C}$ $(c = 1,\ldots,C)$ include C pairs of complex-valued spatial maps and time courses, and $\mathbf{B}^k$ denotes the baseline, $k = 1,\ldots,K$, with K being the number of subjects. We used $C = 8$ and $K = 10$ in this study. Figure 3 shows the magnitude and phase templates of eight complex-valued spatial maps and their associated time courses. C1–C7 correspond to the medial visual areas (VIS), DMN, cerebellum, sensorimotor (MOT), auditory cortex (AUD), right and left frontoparietal components, respectively (Smith et al., 2009), and C8 is a noisy component.

The activations in the spatial maps were formed by the sphere with randomly reduced size (<20%) at its edge for different subjects. The sphere activations had the same center location for the magnitude and phase maps of a complex-valued component, but 5% larger radius for the phase map than for the magnitude map. For C1–C7, the magnitude maps consisted of activation voxels within [0.5, 10] satisfying exponential distribution and the phase maps included signal voxels with small phase changes within $[-\pi/4, \pi/4]$ satisfying Gaussian distribution, as shown in Figure 3a(1) and b(1). The other noisy voxels of magnitude maps were within [0, 3] with Rayleigh distribution and those of the phase maps were with large phase changes ($[-\pi, -\pi/4)$ and $(\pi/4, \pi]$) following exponential distribution. The noisy component C8 was formed by uniformly distributed noisy voxels for both the

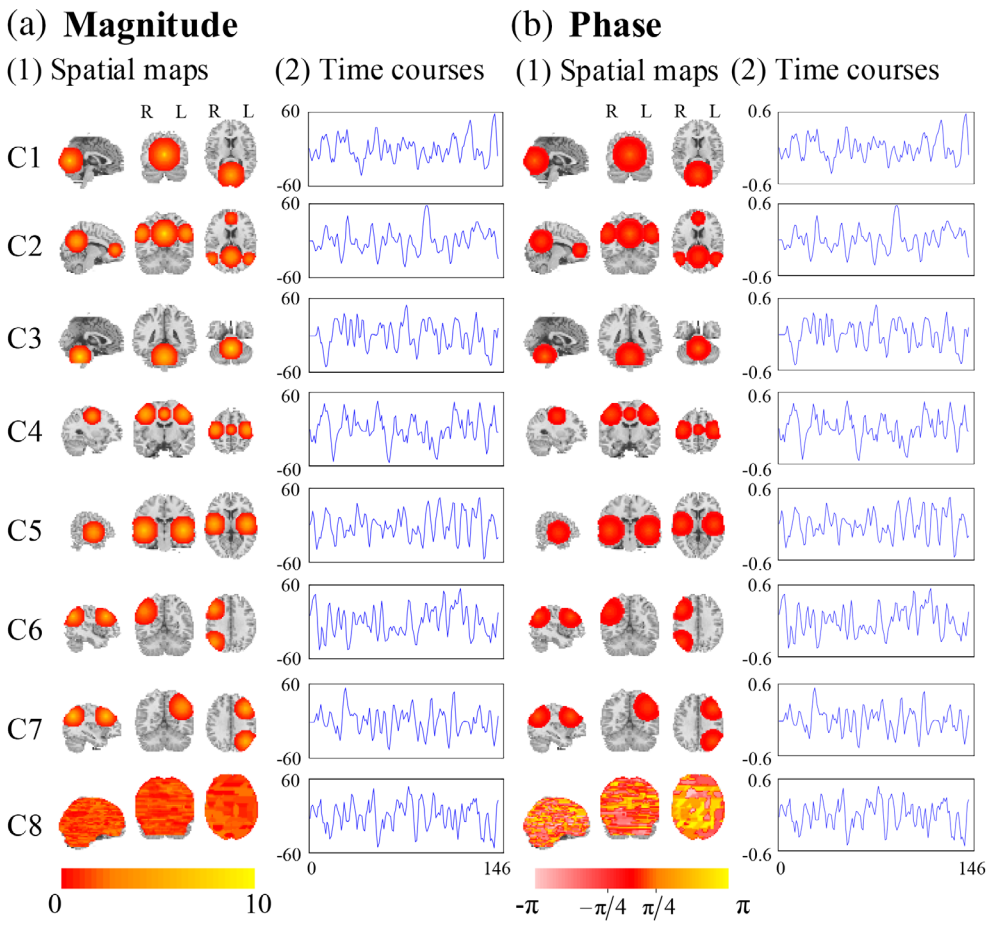

FIGURE 3 Eight simulated resting-state complex-valued components. (a) Magnitude, (b) phase; (1) spatial maps, (2) time courses. C1–C7 correspond to medial visual areas, DMN, cerebellum, sensorimotor, auditory cortex, right and left frontoparietal, and C8 is a noisy component.

magnitude (within [0, 3]) and phase (within $[-\pi, -\pi/4)$ and $(\pi/4, \pi]$) maps. The time courses of C1–C8, as shown in Figure 3a(2) and b(2), were generated based on the resting-state model and default parameters used in SimTB (Erhardt et al., 2012). The magnitude and phase of each complex-valued time course had the same waveform, consisting of random and unique events, and each unique event occurred with a probability of .5 at each TR with an amplitude of 1. The difference was that the amplitude of the magnitude time course was 100 times larger than that of the phase time course. We set the total number of time points $T = 146$ and TR = 2 s to simulate the experimental complex-valued fMRI data. To increase differences among 10 subjects, we used different baseline $\mathbf{B}^k$, which was the averaged experimental complex-valued fMRI signal across all time points from 10 healthy controls.

Next, we added Gaussian noise to the real and imaginary parts of above-generated complex-valued data $\mathbf{Z}^k$, in terms of contrast-to-noise ratio (CNR) defined as $20\log(\sigma_s/\sigma_n)$, where σ_s and σ_n are the temporal standard deviation of the true signal and the noise (Erhardt et al., 2012). The noisy data were with five levels of CNRs: −25, −20, −15, −10, −5 dB. Finally, the magnitude and phase images were spatially smoothed with an $8 \times 8 \times 8\,\text{mm}^3$ FWHM Gaussian kernel. Each spatial image had $53 \times 63 \times 46$ voxels with $V = 62{,}336$ in-brain voxels (non-brain voxels were set to zeroes), which was the same as those of the experimental complex-valued spatial images.

2.1.2 | Experimental fMRI data

We used two kinds of experimental fMRI datasets in this study, including complex-valued data from University of New Mexico and magnitude-only data from HCP. First, the complex-valued, resting-state fMRI datasets from UNM have been described in Qiu et al. (2019). These datasets were collected from 82 subjects with written subject consent overseen by the UNM Institutional Review Board. During the scan, all participants were instructed to rest quietly in the scanner, keep their eyes open without sleeping, and not think of anything in particular. fMRI scans were acquired using a 3.0 T Siemens Allegra scanner (Siemens Medical Solutions USA, Inc., Malvern, PA, USA) equipped with 40 mT/m gradients and a standard quadrature head coil. The functional scan was acquired using gradient-echo echo-planar imaging with the following parameters: TR = 2 s, TE = 29 ms, field of view = 24 cm, acquisition matrix = 64 × 64, flip angle = 75°, slice thickness = 3.5 mm, slice gap = 1 mm. The Statistical Parametric Mapping (SPM) software package (http://www.fil.ion.ucl.ac.uk/spm) was used in data preprocessing. Five scans were excluded because of steady-state magnetization effects. Functional images were motion corrected and then spatially normalized into the standard Montreal Neurological Institute (MNI) space. In spatial normalization, the data were slightly resampled to $3 \times 3 \times 3\,\text{mm}^3$, resulting in $53 \times 63 \times 46$ voxels. Both the magnitude and phase images were spatially smoothed with an $8 \times 8 \times 8\,\text{mm}^3$ FWHM Gaussian kernel. The phase images were first motion corrected using the transformations computed from the magnitude data; next, complex division of the phase data by the first time point reduced the need for phase unwrapping; and spatial normalization of the phase images used the warp parameters computed from the magnitude-only data. A total of 146 scans (i.e., time points $T = 146$) and $V = 62{,}336$ in-brain voxels per subject were entered into the ICA analysis. In addition to the complex-valued fMRI data, both the magnitude and phase fMRI data are separately used to verify the effectivity of the proposed method.

Second, we used resting-state, magnitude-only fMRI datasets from the WU-Minn (Washington University, the University of Minnesota, and Oxford University) HCP consortium to verify our proposed method. The detail information has been described in Essen et al. (2013) and the reference manual of HCP 1200 Subjects release (S1200 Release, February 2017). S1200 HCP subjects were collected from young healthy adult twins and their non-twin siblings, in the age range of 22–35 years. The first 40 subjects, as shown in Table 1, were selected for testing the proposed method. The fMRI data were scanned on a customized Siemens 3 T "Connectome Skyra" at Washington University, using a standard 32-channel Siemens receive head coil. The functional scan was acquired using gradient-echo EPI imaging with the following parameters: TR = 720 ms, TE = 33.1 ms, field of view = 208 × 180 mm, acquisition matrix = 104 × 90, flip angle = 52°, slice thickness = 2.0 mm, multiband factor = 8, echo spacing = 0.58 ms. The SPM software package was used in data preprocessing. For each subject, the fMRI data were acquired in four runs, two runs in one session and two in another session, with eyes

TABLE 1 The identification (ID) for the 40 subjects used in our experiments.

Subject	ID	Subject	ID	Subject	ID	Subject	ID
1	100206	11	102109	21	103515	31	106016
2	100307	12	102311	22	103818	32	106319
3	100408	13	102513	23	104012	33	106521
4	100610	14	102614	24	104416	34	106824
5	101006	15	102715	25	104820	35	107018
6	101107	16	102816	26	105014	36	107220
7	101309	17	103010	27	105115	37	107321
8	101410	18	103111	28	105216	38	107422
9	101915	19	103212	29	105620	39	107725
10	102008	20	103414	30	105923	40	108020

open with relaxed fixation on a projected bright cross-hair on a dark background (and presented in a darkened room). In this study, we selected the run with oblique axial acquisitions alternated between phase encoding in a left-to-right (LR) direction in the first session. The functional images were motion corrected and spatially normalized into the standard MNI space. Following spatial normalization, the data were resampled to $3 \times 3 \times 3$ mm^3, resulting in $53 \times 63 \times 46$ voxels. The images were finally spatially smoothed with an $8 \times 8 \times 8$ mm^3 FWHM Gaussian kernel. A total of $T = 1200$ scans and $V = 62{,}336$ in-brain voxels per subject were entered into the ICA analysis.

2.2 | Methods

The mapping framework is shown in Figure 4. The input is a real-valued ICA map (a magnitude/phase/magnitude-only map extracted from magnitude/phase/magnitude-only fMRI data), and the output is the mathematical SSP map. A mapping function is first learned and then used to transform a processed ICA map into its corresponding mathematical SSP map. The ICA map processing consists of polarity correction and *z*-score normalization, as required by amplitude-based thresholding, followed by denoising (square, smooth, root) to increase the distribution similarity to the SSP map (super-Gaussian with high percentage of large phase voxels, referring to Section 4.2). We select a generalized Gaussian function to form the mapping function, and estimate its shape and scale parameters using maximum likelihood estimation (MLE), based on augmented voxels (symmetrically adding negative values for each voxel) in the denoised ICA map. The amplitude of mapping function is finally adjusted to $[0, \pi]$ to generate the mathematical SSP map. Below we provide the details of the proposed method.

2.2.1 | Polarity correction and *z*-score normalization

Given observed phase or magnitude fMRI data from a single subject $\mathbf{Z} \in \mathbb{R}^{T \times V}$, where T is the total number of time points, and V is the number of in-brain voxels. The model of ICA is $\mathbf{Z} = \mathbf{AS}$, where $\mathbf{S} = \{\mathbf{s}_n\} \in \mathbb{R}^{N \times V}$ and $\mathbf{A} = \{\mathbf{a}_n\} \in \mathbb{R}^{T \times N}$ ($n = 1, \ldots, N$) include N pairs of real-valued spatial and temporal components, and N is the model order (i.e., the number of components). One can select an algorithm such as Infomax (Bell & Sejnowski, 1995) to perform ICA on $\mathbf{Z}$ and obtain N estimates of spatial components denoted as $\widehat{\mathbf{s}} = \{\widehat{\mathbf{s}}_n\} \in \mathbb{R}^{N \times V}$.

We then select a component of interest using the maximum correlation principle $\max\{|\mathrm{corr}(\widehat{\mathbf{s}}_n, \mathbf{s}_{\mathrm{ref}})|\}$, where "corr" denotes the correlation coefficient between two vectors, $\mathbf{s}_{\mathrm{ref}}$ is the spatial reference for the component of interest. The mostly used spatial references are the resting state networks obtained in Allen et al. (2011) and Smith et al. (2009).

Assuming $\widehat{\mathbf{s}}$ denotes the spatial component of interest (i.e., the real-valued ICA map in Figure 4), its polarity may invert activations (negative) and noise (positive) due to the sign ambiguity of ICA, resulting in the removal of all activations as insignificant voxels (*z*-score < 0.5). Thus, we first correct the polarity of $\widehat{\mathbf{s}}$ as follows:

$$\widehat{\mathbf{s}} = \begin{cases} \widehat{\mathbf{s}}, & \text{if } \mathrm{corr}(\widehat{\mathbf{s}}, \mathbf{s}_{\mathrm{ref}}) \geq 0 \\ -\widehat{\mathbf{s}}, & \text{otherwise} \end{cases}. \tag{2}$$

Z-score normalization is performed for the polarity corrected component $\widehat{\mathbf{s}}$ as follows:

$$\overline{\mathbf{s}} = \frac{\widehat{\mathbf{s}} - \mathrm{mean}(\widehat{\mathbf{s}})}{\mathrm{std}(\widehat{\mathbf{s}})}, \tag{3}$$

where "mean" and "std" denote the mean and standard deviation of $\widehat{\mathbf{s}}$, respectively.

2.2.2 | Denoising via squaring, smoothing and rooting

Next, we denoise the polarity corrected and *z*-score normalized ICA map $\overline{\mathbf{s}}$ to increase the number of large phase voxels to remove as many noisy voxels as possible, that is, to have similar super-Gaussian distribution to the SSP map. We propose to incorporate squaring and rooting into spatial smoothing to improve the denoising. The squaring is used to widen the amplitude gap between signal and noisy voxels by enhancing the continuity of larger activations, and the rooting together with spatial smoothing incorporates this merit into the denoised ICA map. As a result, the percentage of large phase voxels is increased to largely remove noisy voxels.

The denoising for the polarity corrected and *z*-score normalized ICA map is expressed as follows:

$$\widetilde{\mathbf{s}} = \sqrt{\mathrm{smooth}\left(\overline{\mathbf{s}}^2\right)}, \tag{4}$$

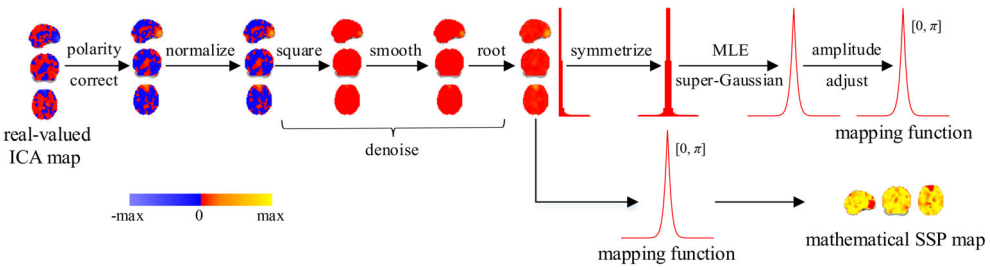

FIGURE 4 The mapping framework for generating mathematical SSP map from a real-valued ICA map.

where "smooth" denotes the 3D spatial smoothing in a neighborhood with a pre-defined full width at half-maximum (FWHM) Gaussian kernel, and the voxels in the denoised ICA map $\widetilde{\mathbf{s}} = \{\widetilde{s}_v\}_{v=1}^{V}$ are with positive values. When generating the mapping function, we need a symmetrical distribution from $\widetilde{\mathbf{s}} = \{\widetilde{s}_v\}_{v=1}^{V}$ with both positive and negative values. As such, we remove the minimum voxel value $\widetilde{s}_{v,\min}$ for each voxel to eliminate the gap between the positive and sequentially augmented negative values. Finally, $\widetilde{\mathbf{s}} = \{\widetilde{s}_v - \widetilde{s}_{v,\min}\}_{v=1}^{V}$ is used in the next step.

2.2.3 | Distribution symmetrizing and mapping function estimation

Similar to the fact that the ICA phase/magnitude maps exhibit the super-Gaussian distribution (see Figures S1–S3), the SSP map also exhibits a super-Gaussian distribution when representing the large phase voxels as a whole via a sharp and strong peak (refer to Figure 14). Thus, we select the generalized Gaussian function with zero mean to form the mapping function as follows:

$$p(x;\boldsymbol{\beta}) = \frac{\beta_2}{2\beta_1\Gamma(1/\beta_2)}\exp\left(-(|x|/\beta_1)^{\beta_2}\right), \tag{5}$$

where $\boldsymbol{\beta} = [\beta_1, \beta_2]^{\mathrm{T}}$ denotes the parameter vector of the function; β_1 is the scale parameter, β_2 is the shape parameter: $\beta_2 < 2$ is super-Gaussian, $\beta_2 = 2$ is Gaussian, $\beta_2 > 2$ is sub-Gaussian; and "$\Gamma(\cdot)$" denotes Gamma function.

Given the augmented voxels of the denoised ICA map, that is, $\widetilde{\mathbf{s}} = \{-\widetilde{s}_v, \widetilde{s}_v\}_{v=1}^{V}$ with symmetrical positive and negative values, we estimate the shape and scale parameters of the mapping function using MLE to avoid the choice of bin width for the least squares fitting of the parametric model. Specifically, we estimate $\boldsymbol{\beta} = [\beta_1, \beta_2]^{\mathrm{T}}$ by maximizing the logarithmic likelihood function of $p(\widetilde{s}_v;\boldsymbol{\beta})$, $v = 1,\ldots,V$ based on Nelder–Mead simplex method (Jeffrey et al., 1998) as follows:

$$\boldsymbol{\beta}_{\mathrm{mle}} = \arg\max_{\boldsymbol{\beta}} \sum_{v=1}^{V} \ln p(\widetilde{s}_v;\boldsymbol{\beta}). \tag{6}$$

With the estimated $\boldsymbol{\beta}_{\mathrm{mle}} = [\beta_{\mathrm{mle},1}, \beta_{\mathrm{mle},2}]$, we obtain the mapping function $p(x;\boldsymbol{\beta}_{\mathrm{mle}})$ from (4).

Finally, we adjust the amplitude range of $p(x;\boldsymbol{\beta}_{\mathrm{mle}})$ from $\left[0, \beta_{\mathrm{mle},2}/\left\{2\beta_{\mathrm{mle},1}\Gamma\left(1/\beta_{\mathrm{mle},2}\right)\right\}\right]$ to $[0, \pi]$ to match the absolute range of SSP values. Let $\gamma = \beta_{\mathrm{mle},2}/\left\{2\beta_{\mathrm{mle},1}\Gamma\left(1/\beta_{\mathrm{mle},2}\right)\right\}$, we have the final mapping function as follows:

$$g(x;\boldsymbol{\beta}_{\mathrm{mle}}) = \frac{\pi\, p(x;\boldsymbol{\beta}_{\mathrm{mle}})}{\gamma}. \tag{7}$$

The mapping function transforms the value of a voxel in $\widetilde{\mathbf{s}}$ into a mathematical SSP value within $[0, \pi]$. Note that we use the range of $[0, \pi]$ instead of $[-\pi, \pi]$, since the polarity of SSP is not explicitly utilized in SSP denoising (Kuang, Lin, Gong, Cong, et al., 2017a; Yu et al., 2015).

2.2.4 | Generation of mathematical SSP and denoising

Given the mapping function $g(x;\boldsymbol{\beta}_{\mathrm{mle}})$ estimated by (6), we can generate the mathematical SSP from a real-valued ICA map. As shown in Figure 4, the input of the mapping function is $\widetilde{\mathbf{s}}$, which is obtained via polarity correction, z-score normalization and denoising (square, smooth, root). The output of the mapping function is the mathematical SSP map. Specifically, taking $\widetilde{\mathbf{s}}$ as the input of the mapping function, the mathematical SSP (shortened as mSSP) is generated as follows:

$$\mathrm{mSSP} = g(\widetilde{\mathbf{s}};\boldsymbol{\beta}_{\mathrm{mle}}), \tag{8}$$

where $\mathrm{mSSP} \in [0, \pi]$. Similar to the SSP denoising approach proposed in Yu et al. (2015), a binary phase mask is generated based on the phase change $\Delta\varphi$ as follows:

$$\mathrm{BM} = \begin{cases} 1, & \text{if } \mathrm{mSSP}(v) \in [0, \Delta\varphi] \\ 0, & \text{otherwise} \end{cases}. \tag{9}$$

Here the baseline phase is 0, and $\Delta\varphi = \pi/4$ is used as the fixed phase change for the denoising. Then, we denoise $\bar{\mathbf{s}}$, i.e., the z-score normalized component, using the binary mask as follows:

$$\underline{\mathbf{s}} = \bar{\mathbf{s}} \circ \mathrm{BM}, \tag{10}$$

where "$\circ$" means the Hadamard product, and $\underline{\mathbf{s}}$ is the mathematical SSP denoised component. A very low z-scores threshold 0.5 was finally used to remove insignificant voxels from $\underline{\mathbf{s}}$.

2.2.5 | Parameter selection and performance measures

We use the Infomax algorithm to perform real ICA of the magnitude/phase/magnitude-only fMRI data with the default parameters provided by the GIFT toolbox (http://trendscenter.org/software/gift/). This algorithm provides a good match to the super-Gaussian distribution of the ICA maps by using the sigmoid nonlinearity as the sore function (Bell & Sejnowski, 1995; Calhoun & Adalı, 2012a, b; McKeown et al., 1998). The model order is $N = 20$ for simulated data and $N = 80$ for experimental data, that is, we separate a total of N components from the fMRI data using ICA. We analyze C1–C7 for simulated fMRI data and select a component of interest named as the anterior cingulate cortex (ACC) for experimental fMRI data based on the spatial reference network detected in Allen et al. (2011). The ACC component was found to be a biomarker region for patients with schizophrenia (Fletcher et al., 1999; Qiu et al., 2019) and can be found in different model orders of ICA. We repeat the ICA separation $R = 10$ times and estimate the best run using the principle of maximum correlation with the reference. We also select the FWHM (i.e., FWHM = $8 \times 8 \times 8$ mm^3) used in the preprocessing of the simulated and experimental fMRI data as a routine procedure.

To make relatively fair comparisons between the two denoising approaches, namely, mathematical SSP denoising and amplitude-based thresholding, we define three kinds of z-scores thresholds within [0.5, 2.5] with an interval of 0.001 for amplitude-based thresholding: (1) to minimize the difference number of total activation voxels (i.e., similar V_{total}) in the two spatial components obtained by the two denoising approaches, denoted as Z_{th1}; (2) to minimize the difference number of activation voxels within the component reference (i.e., similar V_{in}), denoted as Z_{th2}; and (3) to minimize the difference number of activation voxels outside the component reference (i.e., similar V_{out}), denoted as Z_{th3}.

The denoised components by the two denoising methods are evaluated using the following three kinds of indices: (1) the correlation coefficients with the spatial reference for each subject, denoted as ρ, and the mean of ρ over all subjects, denoted as $\overline{\rho}$; (2) the number of activated voxels for each subject in terms of the total voxels V_{total}, the voxels inside the reference V_{in} (i.e., true positive voxels), the voxels outside the reference V_{out} (i.e., false positive voxels), where $V_{total} = V_{in} + V_{out}$, and the mean of V_{in} and V_{out} over all subjects, denoted as $\overline{V}_{in}$ and $\overline{V}_{out}$; (3) the mean of relative differences in V_{in} or V_{out} over all subjects between the two denoising methods with respect to the V_{in} or V_{out} from amplitude-based thresholding (V), denoted as $\Delta V/V$; where $\Delta V/V > 0$ means that mathematical SSP denoising detects ($100\Delta V/V$)% more activated voxels than amplitude-based thresholding, and vice versa.

3 | RESULTS

3.1 | Simulation results

3.1.1 | Single-subject performance

Figures 5 and 6 display DMN (C2) phase and magnitude maps obtained by mathematical SSP denoising (shortened as phase denoising) and amplitude-based thresholding (shortened as amplitude thresholding) at Z_{th1}, Z_{th2} and Z_{th3} from a single-subject simulated fMRI data under CNR $= -25$ dB as an example. Subject 10 was specifically selected due to having a correlation coefficient close to the $\overline{\rho}$ value for the phase and magnitude data, as shown in Figure 7. The threshold for phase denoising was fixed as $\Delta\varphi = \pi/4$, while the thresholds Z_{th1}, Z_{th2} and Z_{th3} for amplitude thresholding were 1.8, 1.41, 2.18 for the phase data and 1.09, 0.88, 1.22 for the magnitude data. From the results of phase data shown in Figure 5, we see that phase denoising obtains much higher ρ value (0.80 vs. 0.68, 0.66, 0.68), and detects 33.91%–80.28% more V_{in} at Z_{th1} and Z_{th3} (2176 vs. 1625, 1207) as well as 69.87%–88.55% fewer V_{out} at Z_{th1} and Z_{th2} (238 vs. 790, 2078) than amplitude thresholding. These results are reasonable when observing the phase mask shown in Figure 5c. It contains more/fewer voxels inside/outside the ground truth (V_{in}: 2196 vs. 2176, V_{out}: 1390 vs. 2078) than the denoised DMN using the lowest amplitude threshold ($Z_{th2} = 1.41$).

The results of magnitude data displayed in Figure 6 verify the conclusion from the phase data. Although phase denoising achieves a similar ρ value (0.92 vs. 0.90, 0.90, 0.91), it detects 7.45%–12.88% more V_{in} at Z_{th1} and Z_{th3} (5362 vs. 4990, 4750) as well as 40.22%–71.28% fewer V_{out} at Z_{th1} and Z_{th2} (556 vs. 930, 1936), compared with amplitude thresholding. The phase mask shown in Figure 6c also defines more BOLD-related voxels but fewer unwanted voxels (V_{in}: 5406 vs. 5363, V_{out}: 1011 vs. 1936) than the spatial map denoised by amplitude thresholding at the lowest threshold ($Z_{th2} = 0.88$).

3.1.2 | Group-level performance

We compare phase denoising using $\Delta\varphi = \pi/4$ and amplitude thresholding using Z_{th1}, Z_{th2} and Z_{th3} at a group level, in terms of $\overline{\rho}$, $\overline{V}_{in}$, $\overline{V}_{out}$, and $\Delta V/V$. Figure 7 displays results averaged across C1–C7 estimated from simulated phase and magnitude data under different CNRs. We observe that phase denoising yields higher $\overline{\rho}$ values, more $\overline{V}_{in}$, but less

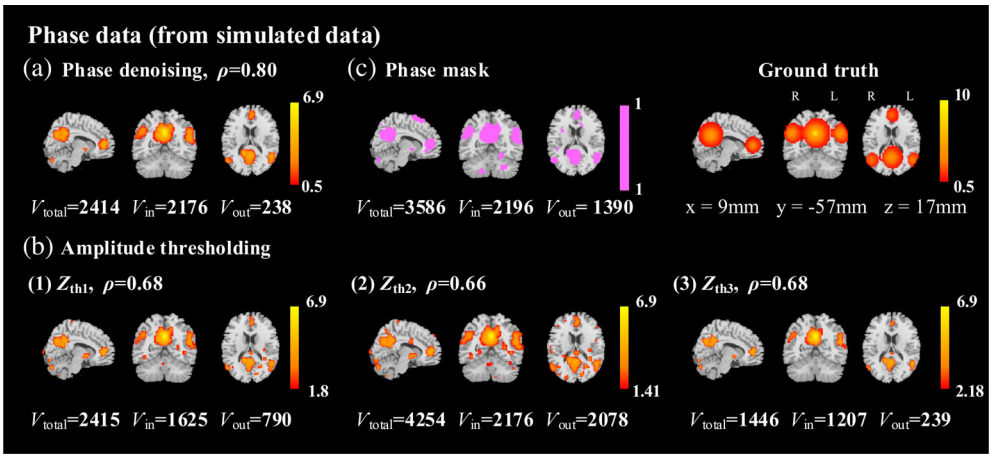

FIGURE 5 A comparison of DMN (C2) phase maps obtained by (a) phase denoising and (b) amplitude thresholding at (1) Z_{th1}, (2) Z_{th2}, and (3) Z_{th3} from the phase of single-subject simulated fMRI data under CNR $= -25$ dB. The binary phase mask generated with $\Delta\varphi = \pi/4$ is shown in (c). The correlation coefficients (ρ) of the denoised DMN with the ground truth component and the number of the total voxels (V_{total}), the voxels inside (V_{in}) and outside (V_{out}) the ground truth component are also shown.

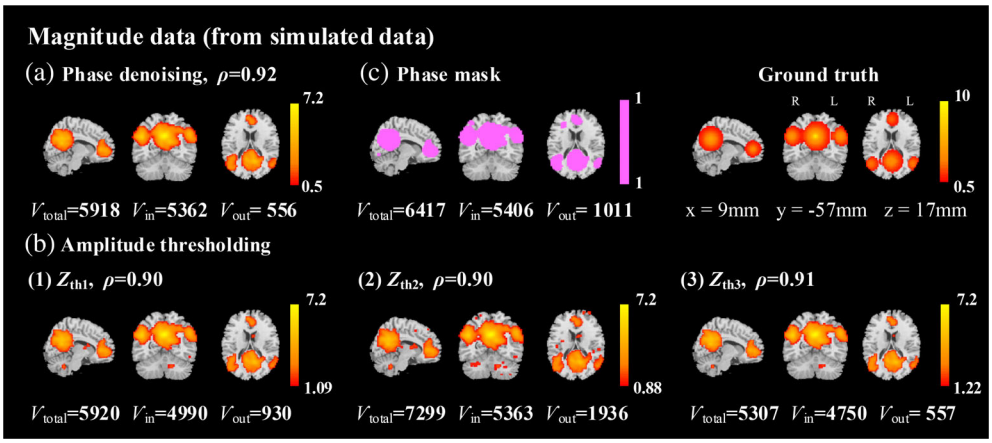

FIGURE 6 A comparison of DMN (C2) magnitude maps obtained by (a) phase denoising and (b) amplitude thresholding at (1) Z_{th1}, (2) Z_{th2}, and (3) Z_{th3} from the magnitude of single-subject simulated fMRI data under CNR = −25 dB. The binary phase mask generated with $\Delta\varphi = \pi/4$ is shown in (c). The correlation coefficients (ρ) of the denoised DMN with the ground truth component and the number of the total voxels (V_{total}), the voxels inside (V_{in}) and outside (V_{out}) the ground truth component are also shown.

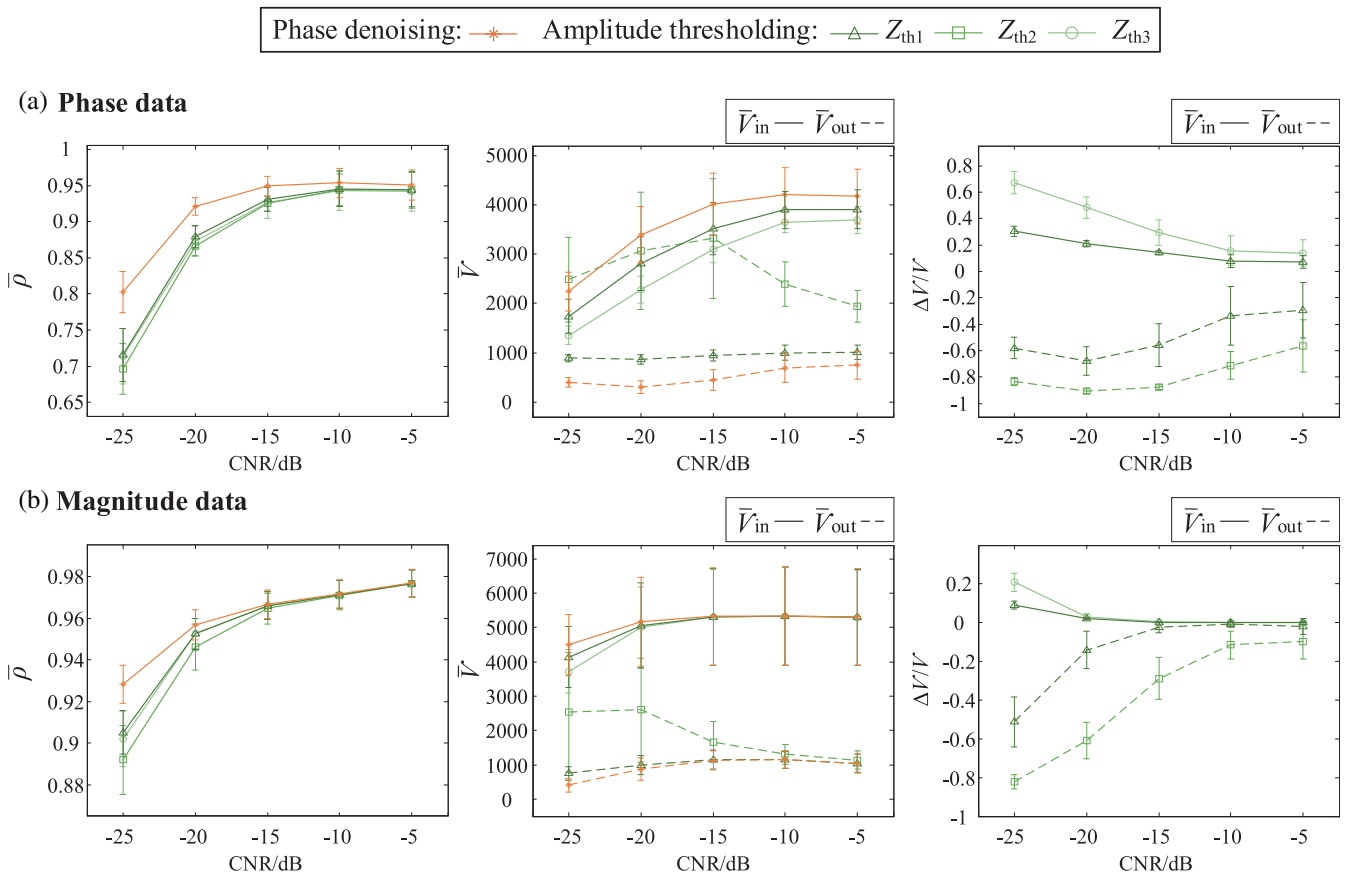

FIGURE 7 A comparison of $\overline{\rho}$, $\overline{V}_{in}$, $\overline{V}_{out}$ and $\Delta V/V$ averaged over C1–C7 obtained by phase denoising and amplitude thresholding at Z_{th1}, Z_{th2}, and Z_{th3} from (a) phase and (b) magnitude simulated fMRI data of all subjects under CNRs = −25, −20, −15, −10, −5 dB. When $\Delta V/V > 0$, phase denoising detects $(100\Delta V/V)$% more activated voxels than amplitude thresholding, and vice versa.

$\overline{V}_{out}$ than amplitude thresholding for both phase and magnitude data, especially for the lower CNRs (CNRs ≤ −5 dB). For the phase data, phase denoising obtains 0.06%–30.31% and 0.08%–67.10% more $\overline{V}_{in}$ ($\Delta V/V > 0$) than amplitude thresholding at Z_{th1} and Z_{th3}, and 0.69%–67.78% and 9.85%–90.40% fewer $\overline{V}_{out}$ ($\Delta V/V < 0$) than amplitude thresholding at Z_{th1} and Z_{th2}. The results on the magnitude data are similar to those from the phase data, except that the performance of phase denoising becomes close to amplitude thresholding at higher CNRs (CNRs > −15 dB), since the magnitude maps were less noisy in these cases.

3.2 | Experimental results

3.2.1 | Complex-valued fMRI data from UNM

Figure 8 displays the ACC component obtained by phase denoising ($\Delta\varphi = \pi/4$) and amplitude thresholding at Z_{th1}, Z_{th2} and Z_{th3} (1.39, 1.08, 1.43) from a single-subject phase fMRI data. Subject 30 was selected to have a correlation coefficient close to the $\bar{\rho}$ value, as shown in Figure 11. We can see that phase denoising yields a similar ρ value (0.30 vs. 0.27, 0.28, 0.27), but detects 23.11%–27.23% more V_{in} at Z_{th1} and Z_{th3} (911 vs. 740, 716) and 7.50%–44.99% fewer V_{out} at Z_{th1} and Z_{th2} (2096 vs. 2266, 3810), compared to amplitude thresholding. The phase mask shown in Figure 8c contains more BOLD-related voxels both within and outside the spatial reference (V_{in}: 1079 vs. 911, V_{out}: 5177 vs. 3810) than the denoised component using the lowest threshold ($Z_{th2} = 1.08$), supporting the advantages of phase denoising over amplitude denoising. Another thing worth noting is that the phase mask defines BOLD-related voxels in terms of the source phase, which is completely different from the amplitude.

When verifying our proposed phase denoising to the magnitude of the complex-valued fMRI data, as shown in Figure 9, the results are similar to those of the phase data. The ACC components were selected from Subject 32 due to a close correlation coefficient to the $\bar{\rho}$ value (see Figure 11). Phase denoising obtains a similar ρ value to amplitude thresholding at $Z_{th1} = 0.94$, $Z_{th2} = 0.76$ and $Z_{th3} = 0.98$ (0.67 vs. 0.66, 0.66, 0.66), but detects more V_{in} and fewer V_{out} than amplitude thresholding. Specifically, phase denoising detects 10.12%–12.55% more V_{in} at Z_{th1} and Z_{th3} (2143 vs. 1946, 1904) and 6.31%–34.10% fewer V_{out} at Z_{th1} and Z_{th2} (2970 vs. 3170, 4507) than amplitude thresholding. The phase mask shown in Figure 9c also defines more BOLD-related voxels than amplitude thresholding at the lowest threshold ($Z_{th2} = 0.76$) both within and outside the spatial reference (V_{in}: 2215 vs. 2143, V_{out}: 5669 vs. 4507). In addition, we provide denoising results of Subject 30 (magnitude data) and Subject 32 (phase data) supplementary to those in Figures 8 and 9 in Figures S4 and S5 for consistency. All the results verify the suitability of the mathematical SSP for denoising magnitude-only components.

To verify the mapping framework shown in Figure 2, we also incorporate the "true" SSP map, the SSP mask and the SSP-denoised magnitude map from the complex-valued fMRI data into Figure 9 as references. This SSP-denoised magnitude map should be similar to but more intact than the magnitude map from the magnitude data of complex-valued fMRI (Figure 9a), due to incorporation of additional activations from the phase data. As expected, the activation regions in the magnitude map, phase mask and mSSP map from the magnitude data (Figure 9a,c,d) are much similar to but smaller than their corresponding references from the complex-valued fMRI data (top row of Figure 9). The overlapping rate is 70% between the masks of mSSP and SSP, and 89.24% between the magnitude maps denoised by mSSP and SSP. By contrast, the three magnitude maps denoised by amplitude thresholding have decreasing overlapping rates (74.45%–83.34%) with the SSP-denoised magnitude map. These results verify the feasibility of the proposed method.

3.2.2 | Magnitude-only fMRI data from HCP

Figure 10 shows comparison of phase denoising and amplitude thresholding for denoising the ACC components estimated from the magnitude-only HCP datasets. The single subject was selected as Subject 34 with a correlation coefficient close to the $\bar{\rho}$ value shown in Figure 11. These results extend those presented in Figures 8 and 9. Phase denoising and amplitude thresholding at $Z_{th1} = 1.11$, $Z_{th2} = 0.68$ and $Z_{th3} = 1.17$ obtain similar ρ values (0.61 vs. 0.58, 0.57, 0.58), as displayed in Figure 10a,b. The differences exist for the number of the detected voxels. Phase denoising detects 20.83%–24.47% more V_{in} at Z_{th1} and Z_{th3} (1816 vs. 1503, 1459) as well as 10.54%–60.83% fewer V_{out} at Z_{th1} and Z_{th2} (2639 vs. 2950, 6737) than amplitude thresholding. As expected, the phase mask shown in Figure 10c defines more

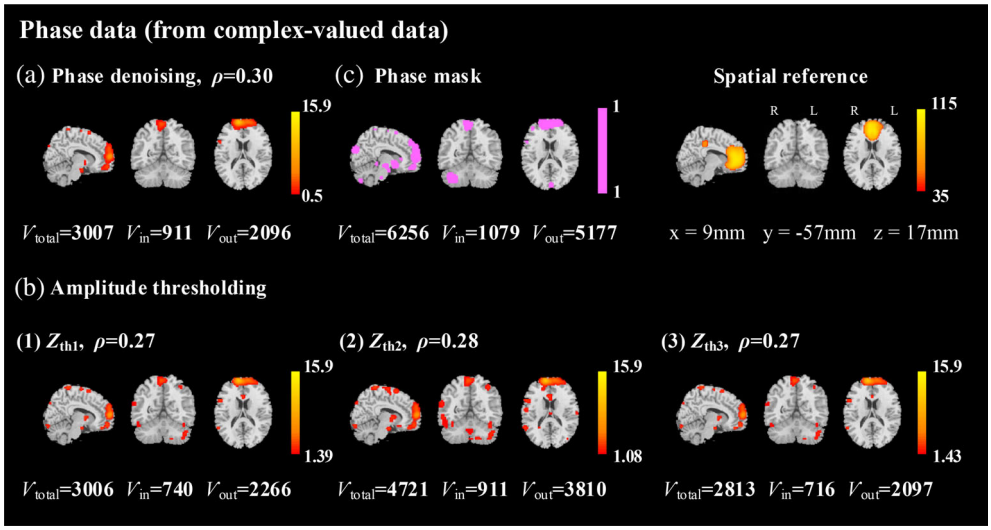

FIGURE 8 A comparison of the ACC components obtained by (a) phase denoising and (b) amplitude thresholding at (1) Z_{th1}, (2) Z_{th2}, and (3) Z_{th3} from the phase of a single-subject complex-valued UNM data. The binary phase mask generated with $\Delta\varphi = \pi/4$ is shown in (c). The correlation coefficients (ρ) of the denoised ACC components with the spatial reference and the number of the total voxels (V_{total}), the voxels inside (V_{in}) and outside (V_{out}) the spatial reference are also shown.

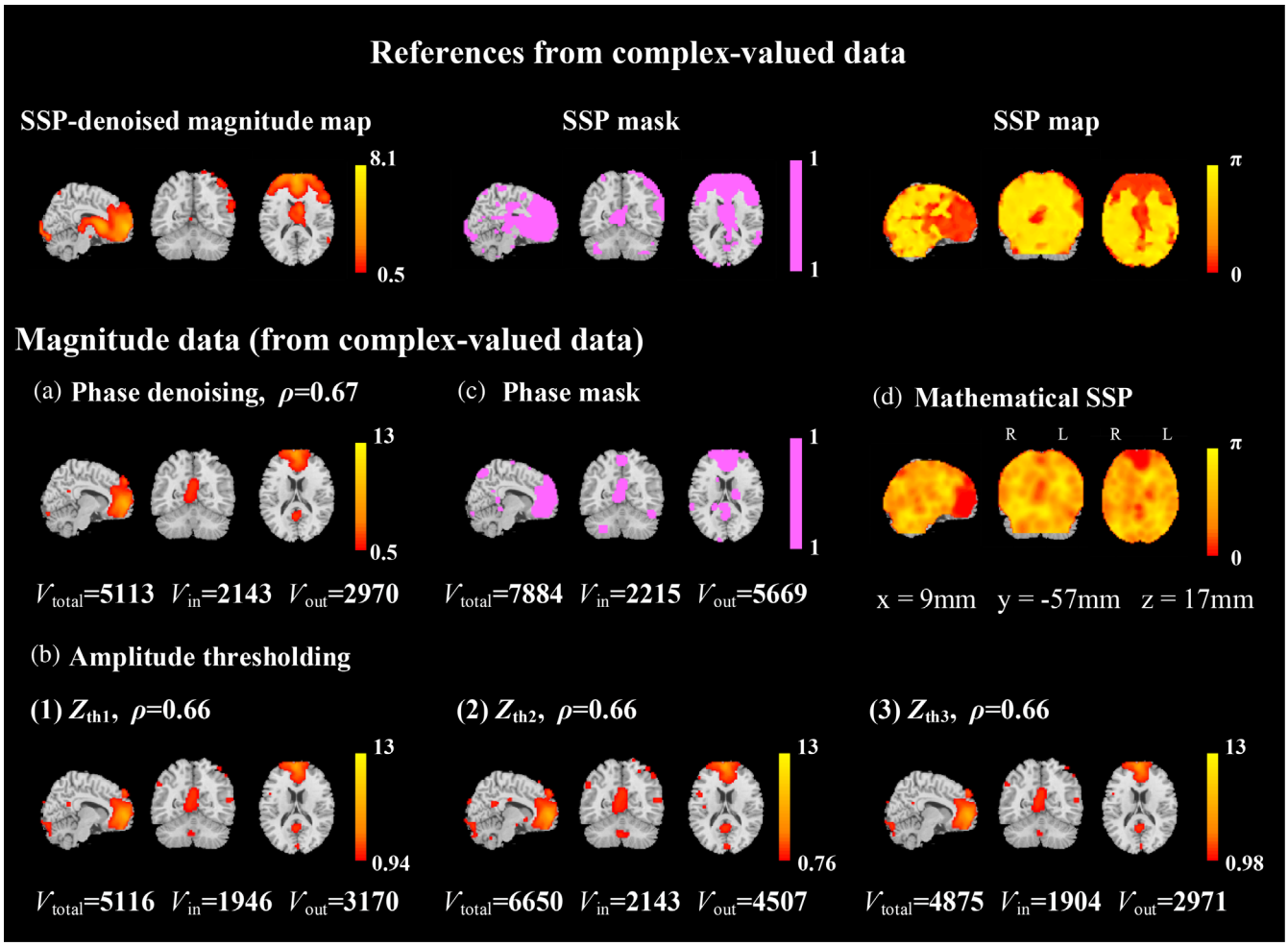

FIGURE 9 A comparison of the ACC components obtained by (a) phase denoising and (b) amplitude thresholding at (1) Z_{th1}, (2) Z_{th2}, and (3) Z_{th3} from the magnitude of a single-subject complex-valued UNM data. The binary phase mask generated with $\Delta\varphi = \pi/4$ is shown in (c), and the generated mathematical SSP (mSSP) is displayed in (d). The top row (from right to left) shows the "true" SSP map, the SSP mask and the SSP-denoised magnitude map from the complex-valued fMRI data. The correlation coefficients (ρ) of the denoised ACC components with the spatial reference and the number of the total voxels (V_{total}), the voxels inside (V_{in}) and outside (V_{out}) the spatial reference are also shown.

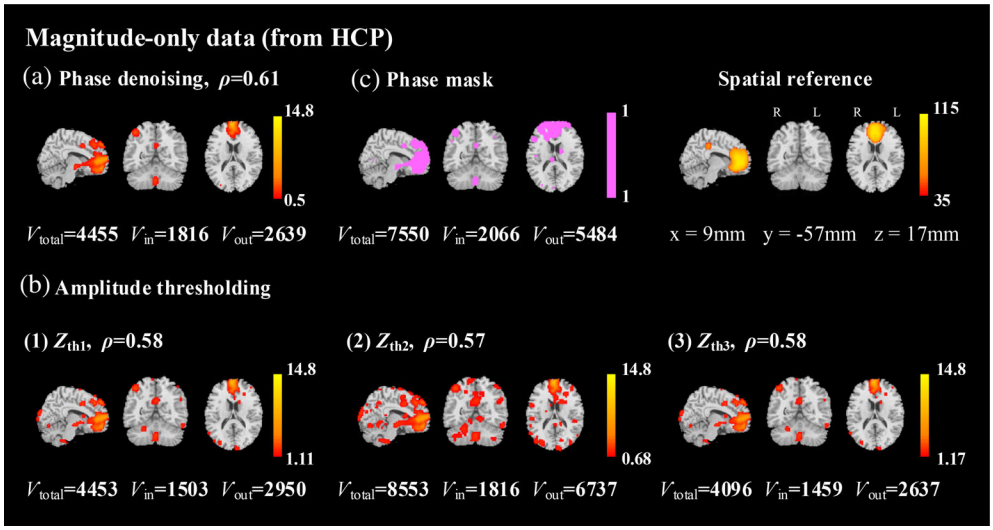

FIGURE 10 A comparison of the ACC components obtained by (a) phase denoising and (b) amplitude thresholding at (1) Z_{th1}, (2) Z_{th2}, and (3) Z_{th3} from a single-subject magnitude-only HCP data. The binary phase mask generated with $\Delta\varphi = \pi/4$ is shown in (c). The correlation coefficients (ρ) of the denoised ACC components with the spatial reference and the number of the total voxels (V_{total}), the voxels inside (V_{in}) and outside (V_{out}) the spatial reference are also shown.

BOLD-related voxels within the spatial reference than amplitude thresholding at the lowest threshold ($Z_{th2} = 0.68$), while defines less outside the spatial reference (V_{in}: 2066 vs. 1816, V_{out}: 5484 vs. 6737).

3.2.3 | Group-level performance

Phase denoising also exhibits better performance than amplitude thresholding at a group level in terms of $\bar{\rho}$, $\bar{V}_{in}$, $\bar{V}_{out}$, and $\Delta V/V$. Figure 11 shows the results from the complex-valued fMRI data (phase and magnitude) and the magnitude-only HCP data. We see that phase denoising yields slightly higher $\bar{\rho}$ values, more $\bar{V}_{in}$, and less $\bar{V}_{out}$, compared with amplitude thresholding at Z_{th1}, Z_{th2} and Z_{th3}. In addition, we observe that, for the three kinds of fMRI data, phase denoising detects 13.22%–16.27% and 15.49%–19.80% more $\bar{V}_{in}$ ($\Delta V/V > 0$) than amplitude thresholding at Z_{th1} and Z_{th3}, and 3.76%–11.86% and 28.72%–55.69% fewer $\bar{V}_{out}$ ($\Delta V/V < 0$) than amplitude thresholding at Z_{th1} and Z_{th2}. These group-level results highlight the benefit of phase denoising over amplitude thresholding in retaining more BOLD-related voxels while removing more noisy voxels, when denoising the magnitude/magnitude-only ICA spatial maps.

We select the ACC component at $N = 80$ as an example to show the superiority of phase denoising over amplitude thresholding. Similar results can be obtained for other ICA networks such as VIS, DMN, MOT and AUD at different model orders. Figure 12 shows the averaged results of $\bar{\rho}$, $\bar{V}_{in}$, $\bar{V}_{out}$, and $\Delta V/V$ for VIS, DMN, MOT and AUD obtained from the HCP data with model orders $N = 40$, 80 and 120. The spatial references for selecting the four components are from Smith et al., 2009 ($Z_{th} = 1$). As expected, phase denoising yields higher $\bar{\rho}$ values, more $\bar{V}_{in}$, and less $\bar{V}_{out}$, compared with amplitude thresholding at Z_{th1}, Z_{th2} and Z_{th3} for all four components at three model orders. In terms of $\Delta V/V$, phase denoising detects 10.52%–15.05% and 15.80%–21.43% more $\bar{V}_{in}$, as well as 11.26%–20.66% and 34.51%–56.76% fewer $\bar{V}_{out}$ than amplitude thresholding at Z_{th1}, Z_{th3} and Z_{th1}, Z_{th2}, respectively.

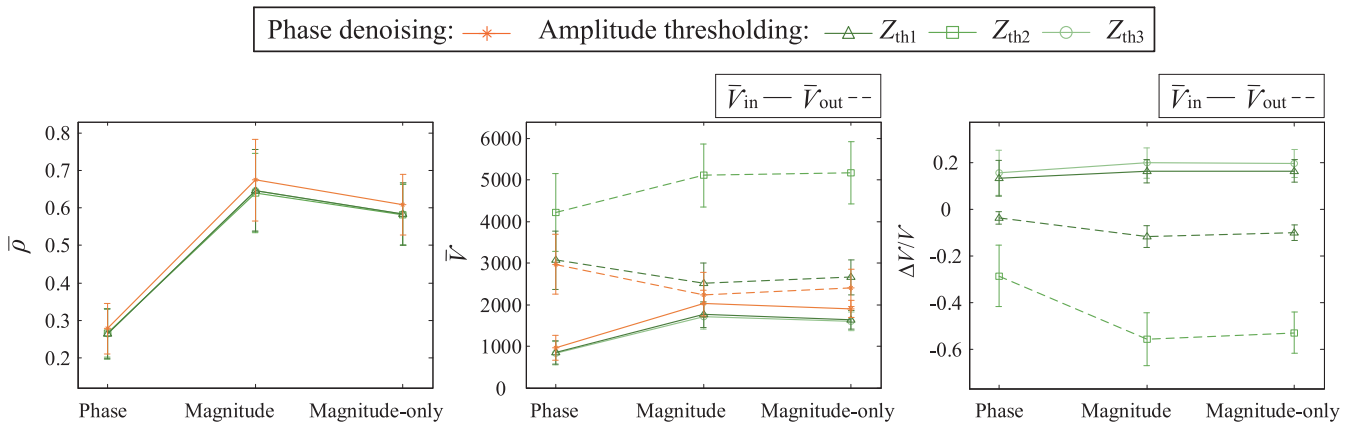

FIGURE 11 A comparison of $\bar{\rho}$, $\bar{V}_{in}$, $\bar{V}_{out}$ and $\Delta V/V$ for the ACC components obtained by phase denoising and amplitude thresholding at Z_{th1}, Z_{th2}, and Z_{th3} from the three experimental fMRI datasets consisting of the phase and magnitude of the complex-valued UNM data and the magnitude-only HCP data.

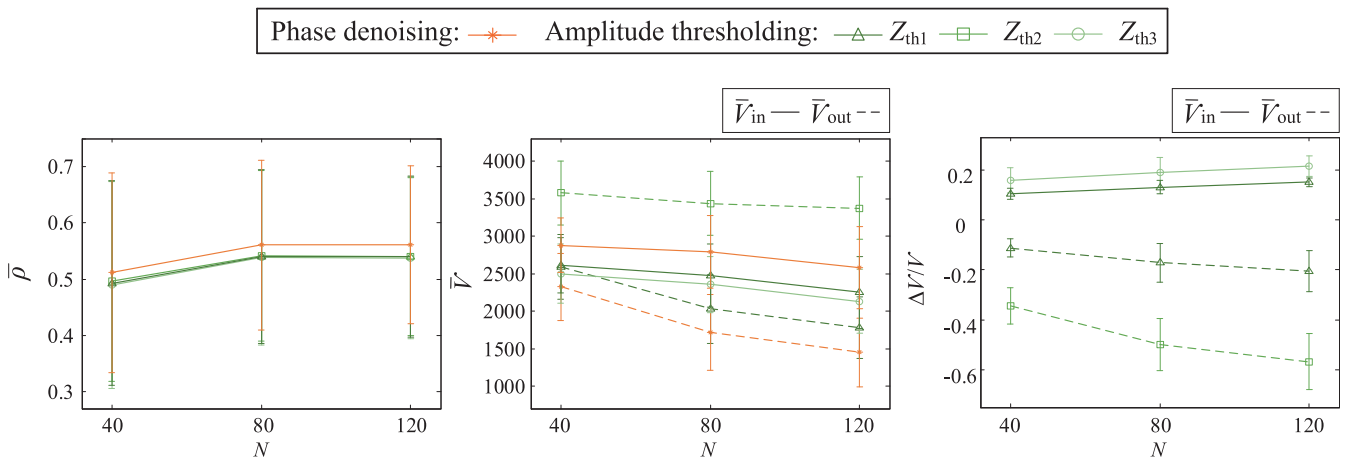

FIGURE 12 A comparison of $\bar{\rho}$, $\bar{V}_{in}$, $\bar{V}_{out}$ and $\Delta V/V$ averaged across VIS, DMN, MOT, and AUD estimated from the HCP data at three different model orders $N = 40$, 80, and 120 and denoised by phase denoising and amplitude thresholding at Z_{th1}, Z_{th2}, and Z_{th3}.

4 | DISCUSSION

4.1 | Effect of a very low *z*-score threshold

It is not an easy thing to define an objective threshold to remove noisy voxels within a component in the analysis of magnitude-only fMRI data. Previously reported *z*-score thresholds are often different in different analyses (e.g., $Z_{th} = 1–3$), and usually larger than 1 (Brookes et al., 2011; Calhoun, Adalı, Pearlson, et al., 2001b; Calhoun & de Lacy, 2017; Correa et al., 2005; Damoiseaux et al., 2007; Jung et al., 2001; Kuang, Lin, Gong, Cong, et al., 2017a; Li et al., 2007; Schwartz et al., 2019; Sui et al., 2012; Yu et al., 2015). By contrast, mSSP denoising uses a fixed phase change ($\pi/4$) to remove the unwanted voxels, followed by further removal of the noisy voxels with a very low *z*-score threshold (i.e., $Z_{th} = 0.5$). Note such a low *z*-score threshold is not acceptable for amplitude-based thresholding, as shown in Figure 13. A large amount of noisy voxels appear in the component when using $Z_{th} = 0.5$, though the correlation coefficients are almost the same as those displayed in Figures 8–10. The results in Figure 13 suggest similar fingerprint capacity of mSSP to SSP in identifying unwanted voxels from BOLD-related voxels, and demonstrate the risk of denoising the brain networks relying only on the voxel amplitude. Note the improvement of the proposed method can increase when using a higher *z*-score threshold such as $Z_{th} = 2.5$ for amplitude-based thresholding. In this case, the number of voxels may significantly decrease for both BOLD-related and unwanted voxels, resulting in the missing of the BOLD-related activations.

4.2 | Effect of denoising (square, smooth, root)

Referring to the mapping framework shown in Figure 4, the similar super-Gaussian distributions to complex SSP were indeed obtained by denoising the normalized ICA map using squaring, smoothing and rooting. Figure 14 shows distributions of the phase maps before and after denoising, and the reorganized and original distribution of complex SSP maps from simulated and experimental fMRI data. It can be seen that the denoised phase maps had more similar distributions to the complex-SSP maps for both datasets. As a result, the denoising increases the number of large phase voxels to remove as many noisy voxels as possible.

In addition, we define the percentage of large phase voxels (PoLPV) at $\Delta\varphi = \pi/4$ to further evaluate the mapping framework as follows:

$$\mathrm{PoLPV}(\pi/4) = \frac{(V_{\mathrm{total}} - V_{0\text{-}\pi/4})}{V_{\mathrm{total}}}, \tag{11}$$

where $V_{0\text{-}\pi/4}$ is the number of voxels with absolute phase values within [0, $\pi/4$], and the large phase denotes the phase values larger than $\pi/4$ for mSSP of a real-valued ICA map or for absolute SSP of a

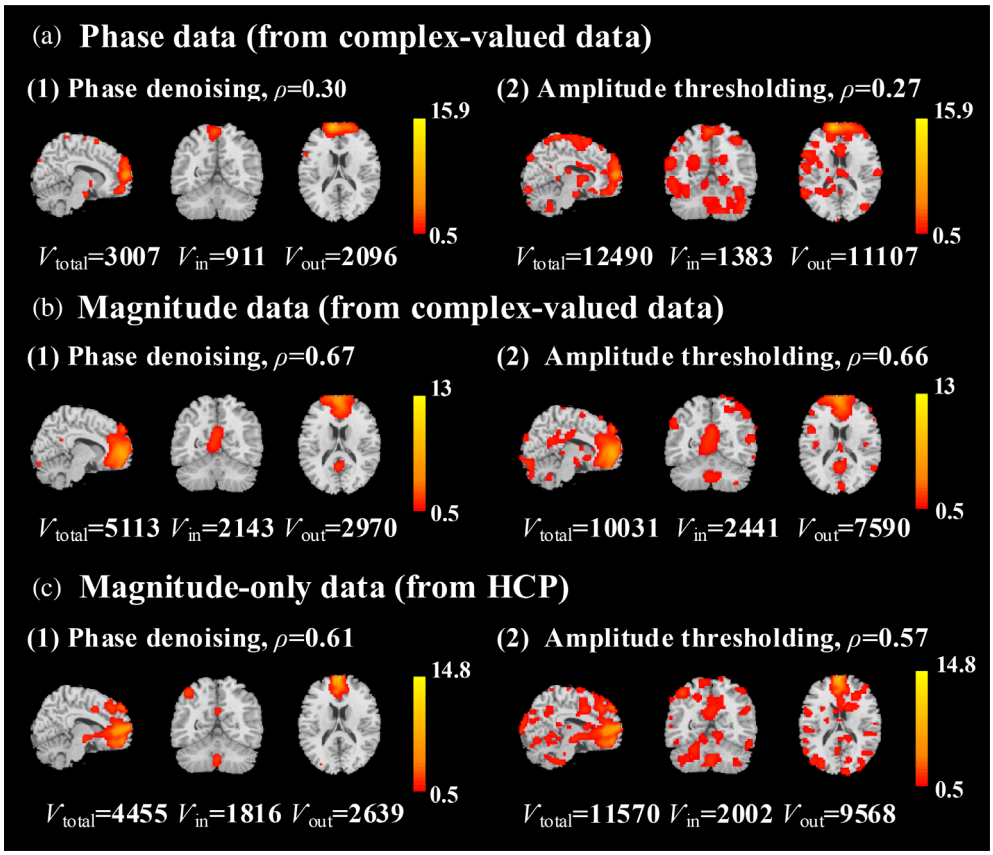

FIGURE 13 A comparison of the ACC components obtained by (a) phase denoising and (b) amplitude thresholding at $Z_{th} = 0.5$ from (a) the phase and (b) the magnitude of single-subject complex-valued UNM data shown in Figures 8 and 9, and (c) single-subject magnitude-only HCP data shown in Figure 10. The correlation coefficients (ρ) with the spatial reference and the number of the total voxels (V_{total}), the voxels inside (V_{in}) and outside (V_{out}) the spatial reference are also shown.

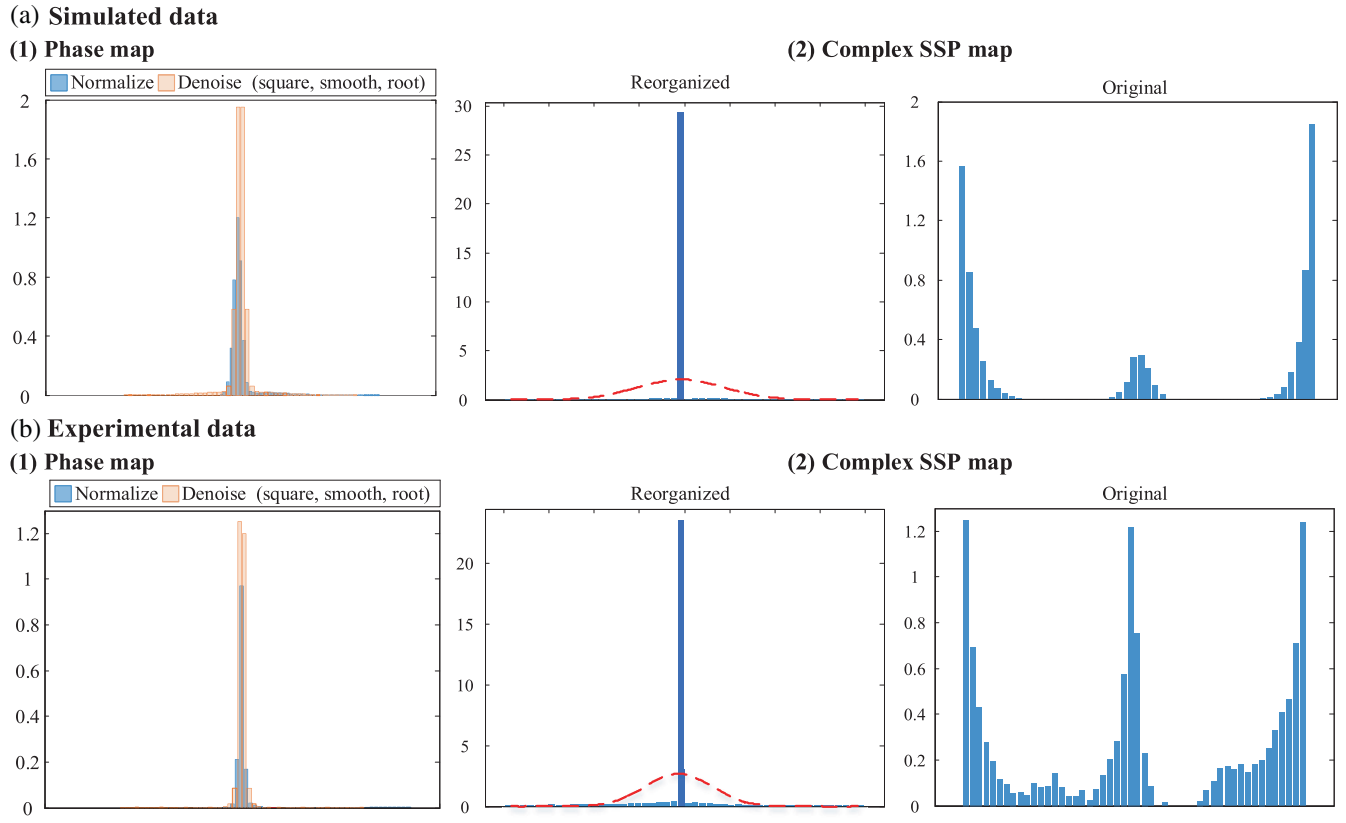

FIGURE 14 The effect of denoising (square, smooth, root) on the distribution of the normalized phase maps from (a) simulated and (b) experimental fMRI data. (1) Phase map before and after denoising. (2) Complex SSP map reorganized by representing the large phase voxels as a whole (left) and the original one (right). For complex SSP map, high bar in dark blue corresponds to unwanted voxels (outside $[-\pi/4, \pi/4]$) while the other bars in light blue correspond to BOLD-related voxels (within $[-\pi/4, \pi/4]$). A Gaussian distribution is shown as a reference.

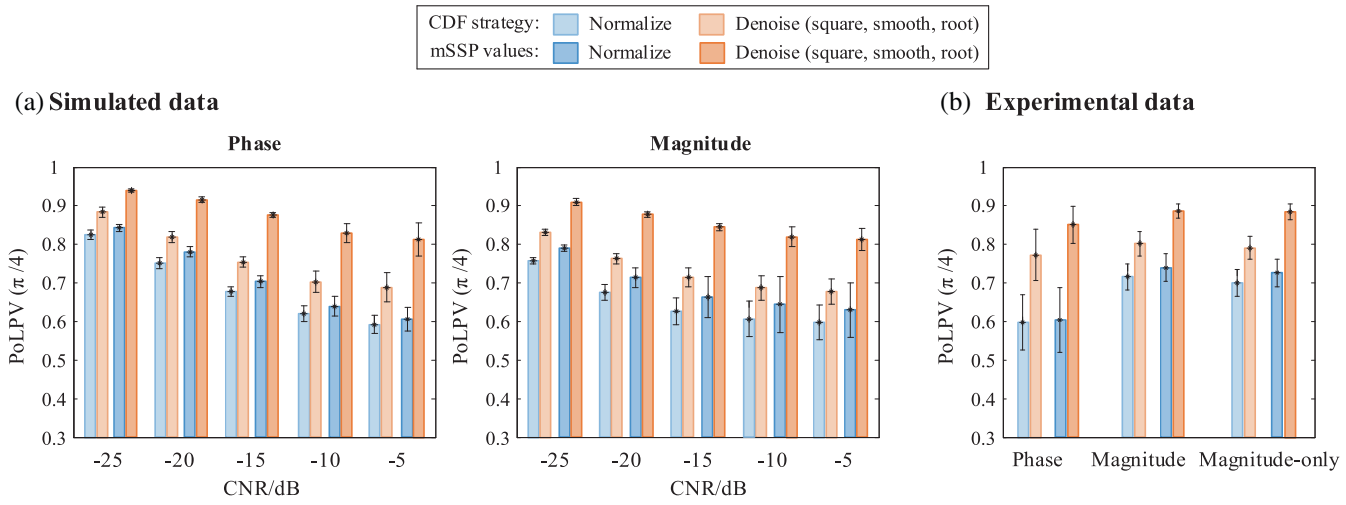

FIGURE 15 A comparison of the percentage of large phase voxels (PoLPV) larger than $\pi/4$ computed by CDF strategy and mSSP values for normalized and denoised (square, smooth, root) ICA maps from (a) simulated and (b) experimental fMRI data. The results in (a) are averaged across C1–C7 maps extracted from simulated phase and magnitude data of all subjects under five CNRs, and the results in (b) are averaged across ACC maps extracted from the phase and magnitude of complex-valued UNM data and the magnitude-only HCP data of all subjects.

complex-valued ICA map. Given the mapping function $g(x;\boldsymbol{\beta}_{\text{mle}})$, we can also compute PoLPV($\pi/4$) using the cumulative distribution function (CDF) strategy as follows:

$$\text{PoLPV}(\pi/4) = \frac{\left\{\int_0^{\infty} g(x;\boldsymbol{\beta}_{\text{mle}})\text{d}x - \int_{g_{\pi/4}}^{\infty} g(x;\boldsymbol{\beta}_{\text{mle}})\text{d}x\right\}}{\int_0^{\infty} g(x;\boldsymbol{\beta}_{\text{mle}})\text{d}x}, \quad (12)$$

where $g_{\pi/4}$ denotes the x value for $g(x;\boldsymbol{\beta}_{\text{mle}}) = \pi/4$, and we indeed use the right half of the mapping function $g(x;\boldsymbol{\beta}_{\text{mle}})$, as shown in Figure 4.

As such, we can verify the effects of denoising (square, smooth, root) in terms of PoLPV ($\pi/4$) computed in two ways: (1) experimental computation using Equation (11); (2) theoretical strategy based on CDF using Equation (12) based on the mSSP values obtained from both simulated and experimental fMRI data. Figure 15 displays the results from the CDF strategy and the mSSP values. We see that the denoising (square, smooth, root) consistently enables the increase of PoLPV, and the PoLPV increase in the mSSP values is higher than that in the CDF values, demonstrating the good performance of mSSP denoising for real-valued ICA maps.

4.3 | Limitations and future work

Although we can detect much more additional activations from the complex-valued fMRI data than from the magnitude-only fMRI data using SSP denoising (Yu et al., 2015), this may not be true by mSSP denoising because of the use of the same fMRI datasets. The mSSP, however, can locate more different BOLD-related voxels both within and outside the spatial reference than the amplitude. The difference is actually derived from the denoising (square, smooth, root) on the real-valued component to match the super-Gaussian distributions of complex SSP, which simultaneously strengthens the amplitude difference between the signal and noisy voxels. As a result, the mSSP achieves similar fingerprint capacity to SSP in terms of detecting more BOLD-related voxels and fewer unwanted voxels than amplitude-based thresholding at moderate z-score thresholds (e.g., Z_{th1}, Z_{th2}, Z_{th3}), as shown in Figures 8–10. Note the amplitude-based thresholding can be improved by using spatial smoothing of the ICA brain networks, but this also leads to the problem of selecting a proper amplitude-based threshold. A phase change unrelated to the amplitude could provide a simple yet effective way for denoising magnitude maps in ICA of fMRI datasets with different signal-to-noise levels. In the future, the differences between mathematical SSP denoising and amplitude-based thresholding can be further investigated by analyzing the magnitude-only fMRI data from patients with mental disorders for improved prediction accuracy.

5 | CONCLUSION

In this study, we propose a mapping framework to generate mathematical SSP (mSSP) for a real-valued ICA brain network based on the assumption that the phase map has a similar distribution with the SSP map from the same component. The resting-state complex-valued simulated fMRI data and two kinds of experimental fMRI datasets, consisting of an 82-subject complex-valued datasets and a 40-subject magnitude-only HCP datasets, were used to evaluate the proposed method. The results show that mSSP denoising can detect more BOLD-related voxels and fewer unwanted voxels, compared with amplitude-based thresholding. Since the parameter selection is minimized in the mapping function estimation, mSSP denoising is a simple yet effective alternative to amplitude-based thresholding in denoising the ICA derived brain networks from magnitude-only fMRI data using a fixed mathematical phase change.

ACKNOWLEDGMENTS

This work was supported in part by the National Natural Science Foundation of China under Grant 61871067, Grant 61379012, Grant 61671106, Grant 62071082, and Grant 81471742; in part by the National Science Foundation (NSF) under Grant 2112455; in part by the National Institutes of Health (NIH) under Grant R01MH104680, Grant R01MH107354, Grant R01EB005846; in part by the Fundamental Research Funds for the Central Universities, China, under Grant DUT20ZD220; and in part by the Supercomputing Center of Dalian University of Technology.

DATA AVAILABILITY STATEMENT

The data that support the findings of this study are openly available in 1200-subjects-data-release at https://www.humanconnectome.org.

ORCID

Qiu-Hua Lin https://orcid.org/0000-0003-0145-7136

REFERENCES

Abou, E. A., Starck, T. J., Nikkinen, J., Tervonen, O., & Kiviniemi, V. (2010). The effect of model order selection in group PICA. *Human Brain Mapping*, *31*(8), 1207–1216.

Acar, E., Schenker, C., Levin, S. Y., Calhoun, V. D., & Adalı, T. (2019). Unraveling diagnostic biomarkers of schizophrenia through structure-revealing fusion of multi-modal neuroimaging data. *Frontiers in Neuroscience*, *13*(5), 416.

Adrian, D. W., Maitra, R., & Rowe, D. B. (2018). Complex-valued time series modeling for improved activation detection in fMRI studies. *Annals of Applied Statistics*, *12*(3), 1451–1478.

Afshin-Pour, B., Grady, C., & Strother, S. (2014). Evaluation of spatio-temporal decomposition techniques for group analysis of fMRI resting state data sets. *NeuroImage*, *87*, 363–382.

Allen, E. A., Erhardt, E. B., Damaraju, E., Gruner, W., Segall, J. M., Silva, R. F., & Calhoun, V. D. (2011). A baseline for the multivariate comparison of resting-state networks. *Frontiers in Systems Neuroscience*, *5*(2), 1–23.

Arja, S. K., Feng, Z., Chen, Z., Caprihan, A., Kiehl, K. A., Adali, T., & Calhoun, V. D. (2010). Changes in fMRI magnitude data and phase data observed in block-design and event-related tasks. *NeuroImage*, *49*(4), 3149–3160.

Beckmann, C. F., & Smith, S. M. (2005). Tensorial extensions of independent component analysis for multisubject fMRI analysis. *NeuroImage*, *25*(1), 294–311.

Bell, A., & Sejnowski, T. (1995). An information-maximization approach to blind separation and blind deconvolution. *Neural Computation*, *7*(6), 1129–1159.

Britz, J., Ville, D. V. D., & Michel, C. M. (2010). BOLD correlates of EEG topography reveal rapid resting-state network dynamics. *NeuroImage*, *52*(4), 1162–1170.

Brookes, M. J., Woolrich, M., Luckhoo, H., Price, D., Hale, J. R., Stephenson, M. C., Barnes, G. R., Smith, S. M., & Morris, P. G. (2011). Investigating the electrophysiology basis of resting state networks using magnetoencephalography. *Proceedings of the National Academy of Sciences*, *108*(40), 16783–16788.

Calhoun, V. D., & Adalı, T. (2012a). Analysis of complex-valued functional magnetic resonance imaging data: Are we just going through a phase? *Bulletin of the Polish Academy of Sciences: Technical Sciences*, *60*(3), 371–387.

Calhoun, V. D., & Adalı, T. (2012b). Multisubject independent component analysis of fMRI: A decade of intrinsic networks, default mode, and neurodiagnostic discovery. *IEEE Reviews in Biomedical Engineering*, *5*, 60–73.

Calhoun, V. D., Adalı, T., Mcginty, V. B., Pekar, J. J., Watson, T. D., & Pearlson, G. D. (2001). FMRI activation in a visual-perception task: Network of areas detected using the general linear model and independent components analysis. *NeuroImage*, *14*(5), 1080–1088.

Calhoun, V. D., Adalı, T., Pearlson, G. D., & Pekar, J. J. (2001a). A method for making group inferences from functional MRI data using independent component analysis. *Human Brain Mapping*, *14*(3), 140–151.

Calhoun, V. D., Adalı, T., Pearlson, G. D., & Pekar, J. J. (2001b). Spatial and temporal independent component analysis of functional MRI data containing a pair of task-related waveforms. *Human Brain Mapping*, *13*(1), 43–53.

Calhoun, V. D., Adalı, T., Pearlson, G. D., Van Zijl, P. C., & Pekar, J. J. (2002). Independent component analysis of fMRI data in the complex domain. *Magnetic Resonance in Medicine*, *48*(1), 180–192.

Calhoun, V. D., & de Lacy, N. (2017). Ten key observations on the analysis of resting-state functional MR imaging data using independent component analysis. *Neuroimaging Clinics of North America*, *27*(4), 561–579.

Calhoun, V. D., Liu, J., & Adalı, T. (2009). A review of group ICA for fMRI data and ICA for joint inference of imaging, genetic, and ERP data. *NeuroImage*, *45*(1 Suppl), S163–S172.

Calhoun, V. D., & Pearlson, G. D. (2012). A selective review of simulated driving studies: Combining naturalistic and hybrid paradigms, analysis approaches, and future directions. *NeuroImage*, *59*(1), 25–35.

Correa, N., Adalı, T., Li, Y., & Calhoun, V. D. (2005). Comparison of blind source separation algorithms for fMRI using a new Matlab toolbox: GIFT. *IEEE international conference on acoustics, speech and signal processing*, Philadelphia (pp. 401–404).

Damoiseaux, J. S., Beckmann, C. F., Arigita, E. J. S., Barkhof, F., Scheltens, P., Stam, C. J., Smith, S. M., & Rombouts, S. A. R. B. (2007). Reduced resting-state brain activity in the "default network" in normal aging. *Cerebral Cortex*, *18*(8), 1856–1864.

Erhardt, E. B., Allen, E. A., Wei, Y., Eichele, T., & Calhoun, V. D. (2012). SimTB, a simulation toolbox for fMRI data under a model of spatio-temporal separability. *NeuroImage*, *59*(4), 4160–4167.

Erhardt, E. B., Rachakonda, S., Bedrick, E. J., Allen, E. A., Adalı, T., & Calhoun, V. D. (2011). Comparison of multi-subject ICA methods for analysis of fMRI data. *Human Brain Mapping*, *32*(12), 2075–2095.

Essen, D. C. V., Smith, S. M., Barch, D. M., Behrens, T. E. J., Yacoub, E., & Ugurbil, K. (2013). The WU-Minn human connectome project: An overview. *NeuroImage*, *80*(80), 62–79.

Feng, Z., Caprihan, A., Blagoev, K. B., & Calhoun, V. D. (2009). Biophysical modeling of phase changes in BOLD fMRI. *NeuroImage*, *47*(2), 540–548.

Fletcher, P., Mckenna, P. J., Friston, K. J., Frith, C. D., & Dolan, R. J. (1999). Abnormal cingulate modulation of fronto-temporal connectivity in schizophrenia. *NeuroImage*, *9*(3), 337–342.

Ge, R., Yao, L., Zhang, H., & Long, Z. (2015). A two-step super-Gaussian independent component analysis approach for fMRI data. *NeuroImage*, *118*, 344–358.

Goebel, R., Esposito, F., & Formisano, E. (2006). Analysis of functional image analysis contest (FIAC) data with brainvoyager QX: From single-subject to cortically aligned group general linear model analysis and self-organizing group independent component analysis. *Human Brain Mapping*, *27*(5), 392–401.

Gopinath, K. S., Sakoglu, U., Crosson, B. A., & Haley, R. W. (2019). Exploring brain mechanisms underlying Gulf War Illness with group ICA based analysis of fMRI resting state networks. *Neuroscience Letters*, *701*, 136–141.

Han, Y., Lin, Q. H., Kuang, L. D., Gong, X. F., Cong, F., Wang, Y. P., & Calhoun, V. D. (2022). Low-rank tucker-2 model for multi-subject fMRI data decomposition with spatial sparsity constraint. *IEEE Transactions on Medical Imaging*, *41*(3), 667–679.

HCP. (n.d.). https://www.humanconnectome.org/storage/app/media/documentation/s1200/HCP_S1200_Release_Reference_Manual.pdf.

Iqbal, A., Meziane, M. N., Seghouane, A. K., & Meraim, K. A. (2020). Adaptive complex-valued dictionary learning: Application to fMRI data analysis. *Signal Processing*, *166*, 1–14.

Jeffrey, C. L., James, A. R., Margaret, H. W., & Paul, E. W. (1998). Convergence properties of the Nelder-Mead simplex method in low dimensions. *SIAM Journal of Optimization*, *9*(1), 112–147.

Jung, T., Makeig, S., Mckeown, M. J., Bell, A. J., Lee, T., & Sejnowski, T. J. (2001). Imaging brain dynamics using independent component analysis. *Proceedings of the IEEE*, *89*(7), 1107–1122.

Kuang, L. D., Lin, Q. H., Gong, X. F., Chen, Y. G., Cong, F., & Calhoun, V. D. (2017). Model order effects on independent vector analysis applied to complex-valued fMRI data. *International symposium on biomedical imaging*, Melbourne (pp. 81–84).

Kuang, L. D., Lin, Q. H., Gong, X. F., Cong, F., & Calhoun, V. D. (2016). An adaptive fixed-point IVA algorithm applied to multi-subject complex-valued FMRI data. *IEEE international conference on acoustics, speech and signal processing*, Shanghai (pp. 714–718).

Kuang, L. D., Lin, Q. H., Gong, X. F., Cong, F., & Calhoun, V. D. (2017a). Post-ICA phase denoising for resting-state complex-valued fMRI data. *IEEE international conference on acoustics, speech and signal processing*, New Orleans (pp. 856–860).

Kuang, L. D., Lin, Q. H., Gong, X. F., Cong, F., & Calhoun, V. D. (2017b). Adaptive independent vector analysis for multi-subject complex-valued fMRI data. *Journal of Neuroscience Methods*, *281*, 49–63.

Kuang, L. D., Lin, Q. H., Gong, X. F., Cong, F., Sui, J., & Calhoun, V. D. (2015). Multi-subject fMRI analysis via combined independent component analysis and shift-invariant canonical polyadic decomposition. *Journal of Neuroscience Methods*, *256*, 127–140.

Kuang, L. D., Lin, Q. H., Gong, X. F., Cong, F., Sui, J., & Calhoun, V. D. (2018). Model order effects on ICA of resting-state complex-valued fMRI data: Application to schizophrenia. *Journal of Neuroscience Methods*, *304*, 24–38.

Kuang, L. D., Lin, Q. H., Gong, X. F., Cong, F., Wang, Y., & Calhoun, V. D. (2020). Shift-invariant canonical polyadic decomposition of complex-valued multi-subject fMRI data with a phase sparsity constraint. *IEEE Transactions on Medical Imaging*, *39*(4), 844–853.

Li, Y., Adalı, T., & Calhoun, V. D. (2007). Estimating the number of independent components for functional magnetic resonance imaging data. *Human Brain Mapping*, *28*(11), 1251–1266.

Lin, Q. H., Niu, Y. W., Sui, J., Zhao, W. D., Zhuo, C., & Calhoun, V. D. (2022). SSPNet: An interpretable 3D-CNN for classification of schizophrenia using phase maps of resting-state complex-valued fMRI data. *Medical Imaging Analysis*, *79*, 102430.

Long, Z., Chen, K., Wu, X., Reiman, E., Peng, D., & Yao, L. (2009). Improved application of independent component analysis to functional magnetic resonance imaging study via linear projection techniques. *Human Brain Mapping*, *30*(2), 417–431.

McKeown, M. J., Makeig, S., Brown, G. G., Jung, T., Kindermann, S. S., Bell, A. J., & Sejnowski, T. J. (1998). Analysis of fMRI data by blind

separation into independent spatial components. *Human Brain Mapping*, *6*(3), 160–188.
Menon, R. S. (2002). Postacquisition suppression of large-vessel BOLD signals in high-resolution fMRI. *Magnetic Resonance in Medicine*, *47*(1), 1–9.
Mørup, M., Hansen, L. K., Arnfred, S. M., Lim, L., & Madsen, K. H. (2008). Shift-invariant multilinear decomposition of neuroimaging data. *NeuroImage*, *42*(4), 1439–1450.
Nencka, A. S., & Rowe, D. B. (2007). Reducing the unwanted draining vein BOLD contribution in fMRI with statistical post-processing methods. *NeuroImage*, *37*(1), 177–188.
Qi, S., Sui, J., Chen, J., Liu, J., Jiang, R., Silva, R., Iraji, A., Damaraju, E., Salman, M., Lin, D., Fu, Z., Zhi, Z., Turner, J. A., Bustillo, J., Ford, J. M., Mathalon, D. H., Voyvodic, J., McEwen, S., Preda, A., … Calhoun, V. D. (2019). Parallel group ICA+ICA: Joint estimation of linked functional network variability and structural covariation with application to schizophrenia. *Human Brain Mapping*, *40*(13), 3795–3809.
Qin, Y., Li, Y., Sun, B., He, H., Peng, R., Zhang, T., Li, J., Luo, C., Sun, C., & Yao, D. (2018). Functional connectivity alterations in children with spastic and dyskinetic cerebral palsy. *Neural Plasticity*, *2018*, 1–14.
Qiu, Y., Lin, Q. H., Kuang, L. D., Gong, X. F., Cong, F. Y., Wang, Y. P., & Calhoun, V. D. (2019). Spatial source phase: A new feature for identifying spatial differences based on complex-valued resting-state fMRI data. *Human Brain Mapping*, *40*(9), 2662–2676.
Risk, B. B., Matteson, D. S., Ruppert, D., Eloyan, A., & Caffo, B. S. (2013). An evaluation of independent component analyses with an application to resting-state fMRI. *Biometrics*, *70*(1), 224–236.
Rodriguez, P. A., Correa, N. M., Eichele, T., Calhoun, V. D., & Adalı, T. (2011). Quality map thresholding for de-noising of complex-valued fMRI data and its application to ICA of fMRI. *Journal of Signal Processing Systems*, *65*(3), 497–508.
Rowe, D. B. (2005). Modeling both the magnitude and phase of complex-valued fMRI data. *NeuroImage*, *25*(4), 1310–1324.
Rowe, D. B. (2009). Magnitude and phase signal detection in complex-valued fMRI data. *Magnetic Resonance in Medicine*, *62*(5), 1356–1357.
Rowe, D. B., & Logan, B. R. (2004). A complex way to compute fMRI activation. *NeuroImage*, *23*(3), 1078–1092.
Schwartz, L. Y., Calhoun, V. D., & Adalı, T. (2019). A method to compare the discriminatory power of data-driven methods: Application to ICA and IVA. *Journal of Neuroscience Methods*, *311*, 267–276.
Shi, Y., & Zeng, W. (2018). SCTICA: Sub-packet constrained temporal ICA method for fMRI data analysis. *Computers in Biology and Medicine*, *102*, 75–85.
Shi, Y., Zeng, W., Tang, X., Kong, W., & Yin, J. (2018). An improved multi-objective optimization-based CICA method with data-driver temporal reference for group fMRI data analysis. *Medical & Biological Engineering & Computing*, *56*(4), 683–694.
Smith, S. M., Fox, P. T., Miller, K. L., Glahn, D. C., Fox, P. M., Mackay, C. E., Filippini, N., Watkinsa, K. E., Toro, R., Laird, A. R., & Beckmanna, C. F. (2009). Correspondence of the brain's functional architecture during activation and rest. *Proceedings of the National Academy of Sciences*, *106*(31), 13040–13045.
Song, J. Y., Qi, M. Y., Lv, D. P., Zhang, C. Y., Lin, Q. H., & Calhoun, V. D. (2021). Sparse representation of complex-valued fMRI data based on hard thresholding of spatial source phase. *IEEE international conference on acoustics, speech and signal processing (ICASSP)*, Toronto (pp. 1105–1109).
Sui, J., Adalı, T., Yu, Q., Chen, J., & Calhoun, V. D. (2012). A review of multivariate methods for multimodal fusion of brain imaging data. *Journal of Neuroscience Methods*, *204*(1), 68–81.
Tomasi, D. G., & Caparelli, E. C. (2007). Macrovascular contribution in activation patterns of working memory. *Journal of Cerebral Blood Flow and Metabolism*, *27*(1), 33–42.
Wolf, I., Dziobek, I., & Heekeren, H. R. (2010). Neural correlates of social cognition in naturalistic settings: A model-free analysis approach. *NeuroImage*, *49*(1), 894–904.
Wu, L., & Calhoun, V. (2023). Joint connectivity matrix independent component analysis: Auto-linking of structural and functional connectivities. *Human Brain Mapping*, *44*(4), 1533–1547.
Yu, M. C., Lin, Q. H., Kuang, L. D., Gong, X. F., Cong, F., & Calhoun, V. D. (2015). ICA of full complex-valued fMRI data using phase information of spatial maps. *Journal of Neuroscience Methods*, *249*, 75–91.
Yu, C. H., Prado, R., Ombao, H., & Rowe, D. (2018). A Bayesian variable selection approach yields improved detection of brain activation from complex-valued fMRI. *Journal of the American Statistical Association*, *113*(524), 1395–1410.
Yu, C. H., Prado, R., Ombao, H., & Rowe, D. (2022). Bayesian spatiotemporal modeling on complex-valued fMRI signals via kernel convolutions. *Biometrics*, *79*(2), 616–628.
Zhou, G., Zhao, Q., Zhang, Y., Adalı, T., Xie, S., & Cichocki, A. (2016). Linked component analysis from matrices to high-order tensors: Applications to biomedical data. *Proceedings of the IEEE*, *104*(2), 310–331.

SUPPORTING INFORMATION

Additional supporting information can be found online in the Supporting Information section at the end of this article.

How to cite this article: Zhang, C.-Y., Lin, Q.-H., Niu, Y.-W., Li, W.-X., Gong, X.-F., Cong, F., Wang, Y.-P., & Calhoun, V. D. (2023). Denoising brain networks using a fixed mathematical phase change in independent component analysis of magnitude-only fMRI data. *Human Brain Mapping*, 1–17. https://doi.org/10.1002/hbm.26471